Nanostructuring Magnetic Thin Films Using Interference Lithography

by

Michael E. Walsh

Submitted to the Department of Electrical Engineering and Computer Science
in partial fulfillment of the requirements for the degree of

## Master of Science in Electrical Engineering

at the
MASSACHUSETTS INSTITUTE OF TECHNOLOGY

BARKER

August, 2000

September, 2000
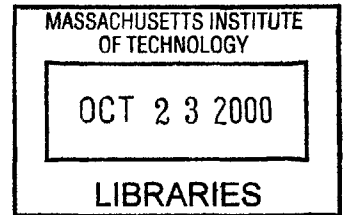
Author...
Department of Electrical Engineering and Computer Science
August 27, 2000

Certified by...
Henry I. Smith
Keithley Professor of Electrical Engineering
Thesis Supervisor

Certified by...
Caroline A. Ross
Professor of Materials Science and Engineering
Thesis Supervisor

Accepted by...
Arthur C. Smith
Chairman, Department Committee on Graduate Students

Nanostructuring Magnetic Thin Films
Using Interference Lithography

by

Michael E. Walsh

Abstract

Proliferation of data caused by rapid increases in computer power and the rise of the internet have caused an acute need for advanced data storage technology. Patterned magnetic media and magneto-resistive random-access memory (MRAM) can potentially fulfill this need. The technique of interference lithography is examined in the context of patterning ~100 nm size features. An interferometer is designed and built which will allow exposure of gratings and grids with a minimum spatial period of ~170 nm. Etching methods, especially ion-beam etching, or ion milling, is investigated as the optimal choice for patterning sub-100 nm features in thin magnetic films and multi-layer thin film stacks. The advantages and disadvantages of a variety of resist stacks and etch masks are presented. An optimal process for linewidth control and preservation of magnetic properties is found to include a thin phase-shifting resist stack and a tungsten hardmask.

Table of Contents

Table of Figures

Acknowledgements

Although my name is the only one on the cover, an enormous amount of credit belongs to a multitude of people for making this research successful. To my advisors, Hank Smith in EECS and Caroline Ross in Materials Science, I thank you for taking a chance on me. I arrived at MIT with my only knowledge of magnetics learned at the refrigerator, and when someone said "nano" I thought of Mork and Mindy. Your guidance has made me a better scientist and a better person.

Science investigation is field in which the progress of one is always built upon the achievements of others before him. I truly believe that my work would have been impossible without the guidance and mentoring provided by the other students working in the NanoStructures Lab. Juan Fererra, Tim Savas, Mike Lim, Tom Murphy: you guys have taught me everything from basic theory to lab techniques best described as "black art". The lab will be a lonely place as you guys move on, and I know that my work will get harder without your experience to draw on. If I could give out a hero award, it would unquestionably go to Maya Farhoud. The countless hours you spent with me in the lab, holding my hand every step of the way, were priceless. I think the only thing you couldn't teach me was a better sense of fashion.

There is not a single piece of equipment or process in the lab that I have not learned, or learned to do better, from Jim Carter, Jim Daley, and Mark Mondol. The wisdom you guys have collected over the years is truly remarkable.

For contributions of a less technical nature, I am thankful for my lifelong friends Andrew Zuffoletti and Jeff Whittingham. You two have made my house a happy home. Your imaginative and subversive views on the role of nanostructures are a source of inspiration.

Laura Green, your unwavering love and support through every day of this has been a great gift. You never let me forget that there is a wonderful world outside the lab.

Finally, I would like to express my deepest thanks to my family, especially my parents. You have given me the confidence and character to allow me to follow my dreams.

Chapter 1:

Introduction

1.1) Patterned Magnetic Media

In recent years, there has been a rapidly growing interest in the fabrication and study of nanometer-scale magnetic elements[1-9]. The data storage industry in particular stands to benefit greatly from advances in magnetic nanostructures. In recent years, the storage density of data has increased exponentially, while the cost per bit of stored data has decreased exponentially. Driving this demand for storage capacity has been the parallel increase in the availability and power of computing technology. With the recent rise of the internet creating an enormous increase in the amount of data available, the need for advanced storage technology has only grown more acute.

Current hard disk technology, which utilizes a continuous magnetic thin film, is believed to have an upper data density limit of about100 Gb/in^2 (1 Gb = 10^9 bits). Data density in state-of-the-art hard drives recently demonstrated by Fujitsu is at 54 Gb/in^2, and advancing rapidly. These bulk films consist of single domain grains 10-20 nm in diameter, with each grain having a randomly oriented magnetic easy axis. To overcome the randomness in grain structure, a bit written into such a film must contain a large number of grains. Figure 1.1a shows the way data bits are stored in todays hard disks. In the expanded view, three neighboring data bits are shown, each comprised of numerous individual grains. The boundary between the bits is jagged, because the grain structure of the film prohibits arbitrarily smooth boundaries.

To increase the number of bits in a given area, either the number of grains per bit must decrease or the grain size itself must decrease. The number of grains per bit can be reduced somewhat by advances in signal

processing, but it is unlikely that this can continue at a sustainable pace. The size of the individual grains can also be decreased, but there is a fundamental limit, known as the superparamagnetic limit, which prevents grain size from becoming arbitrarily small. The superparamagnetic limit is encountered when the magnetic energy of the grain is comparable to thermal energy. Magnetic energy is defined as the net magnetic anisotropy K muliplied by the volume of the grain V, and thermal energy is defined as kT, Boltzmann's constant multiplied by the temperature. If the ratio of magnetic to thermal energy is too low, the magnetization state of the grain can spontaneously reverse, leading to random and uncontrollable data loss [7]. Recent estimates place the KV/kT ratio at around 60 [8].

Conventional Technology   Patterned Media
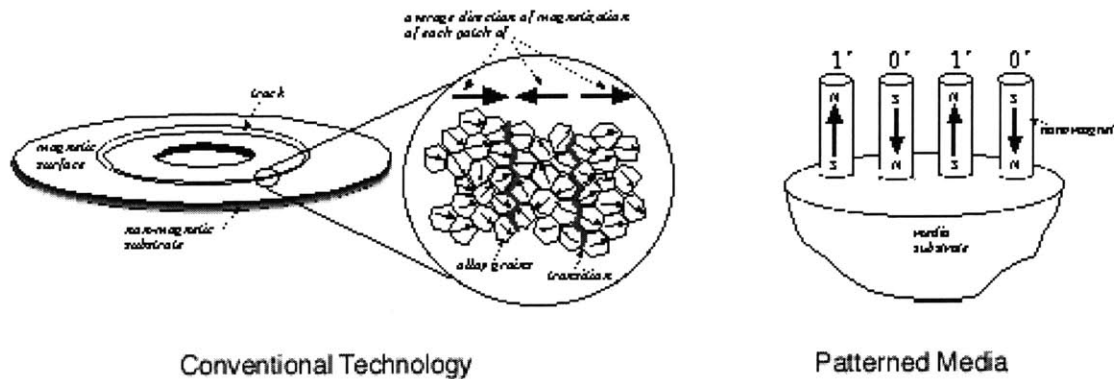
Figure 1.1: *Data storage for conventional hard disk technology is compared to data storage using patterned magnetic media [18].*

Overcoming these two problems will ultimately require a new data storage paradigm. One possible solution is to use patterned magnetic media instead of bulk films, depicted pictorally in Figure 1.1. The use of patterned media allows the bit size to be reduced beyond what is possible using bulk

films. The critical difference in patterned media is that the data bits are defined lithographically and physically separated from one another. Precision of the bit boundaries is now limited by lithography rather than the grain structure of the film, which ideally eliminates media noise [7]. This is because nanometer-scale particles can act as a single magnetic domain if their dimensions are small in comparison to the exchange length of the material [1,5,9] (e.g. λ_{ex}=7 nm for Co and λ_{ex}=20 nm for Ni). The reduction in noise, combined with the fact that each bit can be made into a single magnetic domain eliminates any condition on grain size and the number of necessary grains per bit.

The fundamental limit on bit size when using patterned media is still the superparamagnetic limit. However, in patterned media the limit applies to the size of the entire bit, rather than the grains which make up the bit. Thus, the volume of the whole patterned bit must satisfy KV/kT>60, which is a much less stringent condition than requiring each grain to satisfy KV/kT>60. Estimates place the minimum thermally stable bit size on the order of 10 nm per side (1000 nm^3). The potential data density for bits of this size is >1000 Gb/in^2, providing at least an of magnitude increase over the potential of current technology.

1.2) MRAM Devices

A further possibility that arises when considering patterned magnetic media is the fabrication of high-density magnetic random-access memories (MRAM). Patterned media storage schemes, such as those described in Section 1.1, have magnetically addressable data bits, like a hard drive. However, bits that are electrically addressable are potentially far more valuable. Multi-layer thin film stacks of magnetic and non-magnetic materials can be engineered to exhibit giant magneto-resistance (GMR). Magnetoresistance (MR) is the phenomenon in which the electrical resistance of a material changes with

applied magnetic field and GMR is a high-magnitude MR effect induced in certain multi-layer structures [10,11,12]. In an MRAM device, the electrical resistance of a data bit patterned from a GMR film stack would change with the magnetization state of that bit. Figure 1.2 shows a schematic of a simple multi-layer GMR stack known as a pseudo-spin-valve (PSV). Two layers, a magnetically soft top layer and a magnetically hard lower layer, are separated by a conducting but non-magnetic material. In this case, both layers are the same material, and different thicknesses allow them to switch at different fields. Different materials can also be used for the two magnetic layers. When the magnetization states of both layers are parallel, the electrical resistance is lower than when the two layers are magnetized anti-parallel. Data is stored in the hard magnetic layer, and interrogated by monitoring resistance changes while switching the soft magnetic layer.

High Resistance State
← Switching magnetic layer
Separating conductor
Fixed magnetic layer

Low Resistance State
substrate
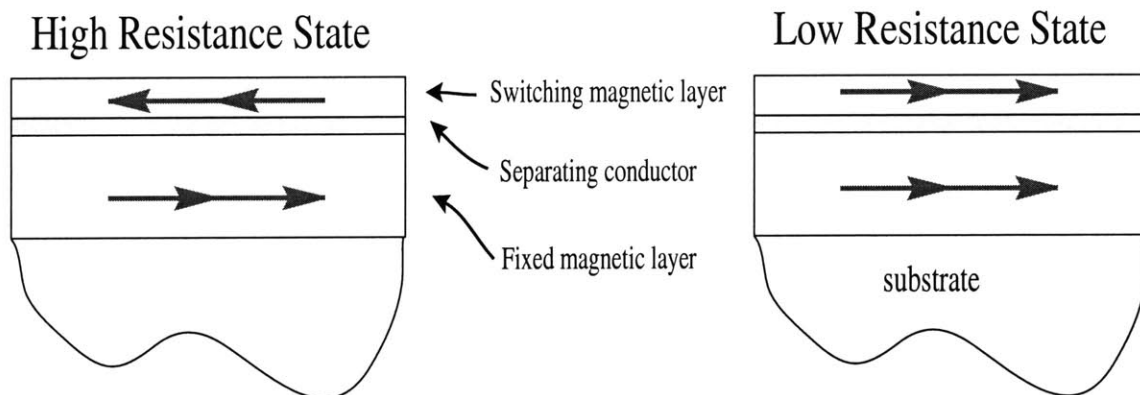
Figure 1.2: *A PSV structure in high and low resistance states.*

A simple potential device incorporating patterned GMR films is seen in Figure 1.3. The GMR elements depicted are designed to exhibit their resistance change perpendicular to the plane, and are placed at the nodes of a grid of crossed conductors. The bit is addressed by selecting the two conducting lines which intersect at that bit. A diode in series with each GMR element would be necessary to limit the current flow only through the intended PSV element. By

sending high or low current pulses through the wires, the bit can be alternately written or read.

The potential for MRAM devices is enormous, in that the capabilities of a hard drive and DRAM could be combined into the same device. In fact, MRAMs have the potential to exceed the capability of either. IBM has demonstrated an MRAM device with read and write times less than 3 ns, which is equivalent to SRAM and much faster than DRAM devices [13]. While semiconductor RAM's are limited by the charging and discharging of capacitors, the switching times of magnetic elements are so fast that the read and write times of magnetic RAMs would be only be limited by the inductance of device wiring. The non-volatilty of MRAM devices also means that they can have much lower power requirements than semiconductor RAM. In an MRAM, energy is only required to read and write the bit, not to maintain it. DRAM devices require continual refreshing of the capacitive elements to maintain stability. The long term data stability of a hard drive would be available in an MRAM, but without large footprint and high operating power. Also, where hard drives have a multitude of moving parts, MRAM devices have none and would be virtually impossible to wear out. [14]

PSV element

conducting wire

conducting wire
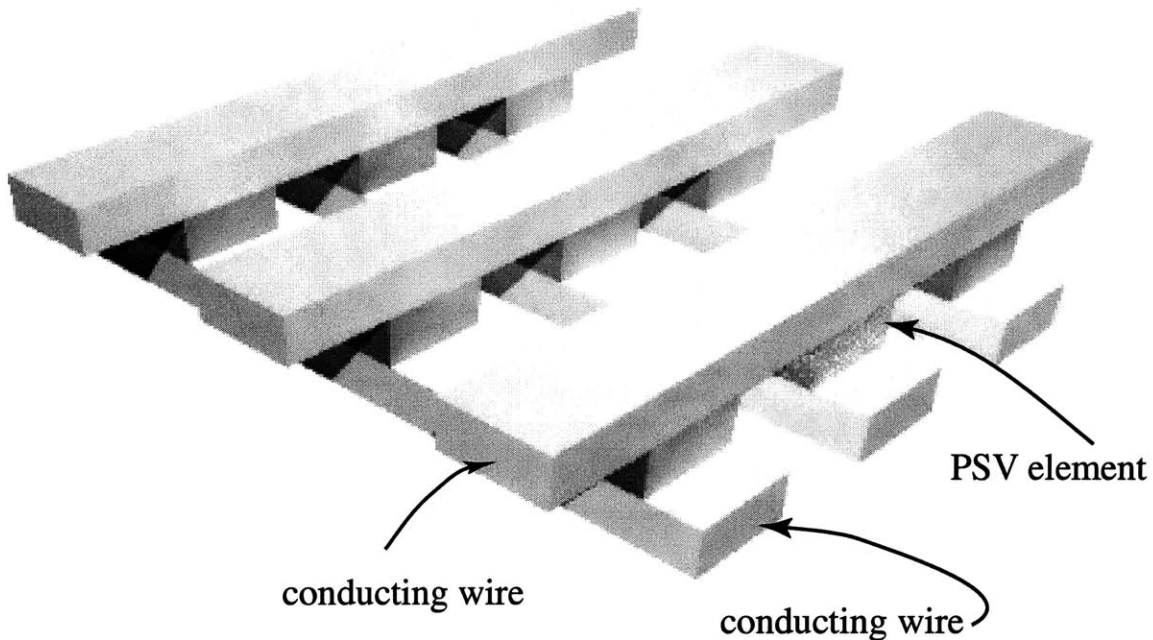
Figure 1.3: *A simple MRAM device with MR elements located at the intersection points of a grid of crossed conductors.*

1.3) Fabrication

Despite the scientific interest and commercial potential of MRAM devices and patterned magnetic media, the necessary fabrication technology is largely unavailable. To achieve a data density high enough to make MRAMs or patterned media practical, feature sizes must be ~100 nm or less. Lithographic capability to date has been driven largely by the semiconductor industry, where the 100 nm size regime is still a number of years away. Also, optical projection lithography is rapidly approaching its limit as a scalable technology; to reach sub-100 nm feature sizes will most likely require a shift to a new lithographic process.

Assuming an appropriate lithographic tool is available, required etch technology for magnetic materials is also underdeveloped. Etch methods with the control necessary for sub-100 nm features, such as reactive-ion etching (RIE), were mainly developed for common semiconductor materials, and do not

work on magnetic materials. Etching of multi-layer structures also presents an unusual challenge.

The work described in this thesis is intended to address the challenge of fabricating nanometer-scale structures in magnetic films and multi-layer magnetic stacks for patterned media and MRAM applications. The equipment and processes described in the following chapters were designed with the intent of being compatible with a variety of magnetic materials, and ever-shrinking linewidth demands. Interference lithography (IL) is presented as an optimal method for producing large-area arrays of sub-100 nm features, and a Lloyds-mirror style interferometer was designed and built to perform the exposures over a wide range of feature sizes more simply than a conventional IL system. The technique of interference lithography can be scaled for smaller features; achromatic interference lithography (AIL) has achieved 50 nm lines and spaces [15] and is proposed for 25 nm lines and spaces [16], while synchrotron radiation has been used to make ~20 nm lines and spaces [17]. Ion-beam etching, or ion milling is shown to be the most versatile technique for etching magnetic nanostructures. A novel process is developed which allows good linewidth control for ~100 nm features and minimizes the negative side-effects associated with ion milling. The combination of IL and ion milling creates a complete fabrication process for nanostructuring a wide variety of magnetic thin films.

1.4) References

[1]   R.P. Cowburn, "Property variation with shape in magnetic nanoelements". J. Phys. D. Appl. Phys. **33** (2000)

[2]   C. Chappert, H. Bernas, J. Ferre, V. Kottler, J.-P Jamet. Y. Chen, E. Cambril, T. Devolder, F. Rousseaux, V. Mathet, H. Launois, "Planar Patterned Magnetic Media Obtained by Ion Irradiation". Science vol. 280 1919 (1998)

[3]   B.D. Terris, L. Folks, D. Weller, J.E.E. Baglin, A.J. Kellock, H. Rothuizen, and P. Vettiger, "Ion-beam patterning of magnetic films using stencil masks". App. Phys. Lett. **75** 403 (1999)

[4]   S.Y. Chou, "Patterned Magnetic Nanostructures and Quantized Magnetic Disks". Proceedings of the IEEE, **85** No. 4, 652 (1997)

[5]   S.Y, Chou, M.S. Wei, P.R. Krauss, P.B. Fischer, "Single-domain magnetic pillar array of 35 nm diameter and 65 Gbits/in.2 density ofr ultrahigh density quantum magnetic storage". J. Appl. Phys. **76** (10) 6673 (1994)

[6]   R.L. White, R.H.M. New, R.F.W. Pease, "Patterned Media" A Viable Route to 50 Gbit/in2 and Up for Magnetic Recording?". IEEE Trans. Magn. **33** 990 (1997)

[7]   C.A. Ross, H.I. Smith, T. Savas, M. Schattenburg, M. Farhoud, M. Hwang, M. Walsh, M.C. Abraham, R.J. Ram, "Fabrication of patterned media for high density magnetic storage". J. Vac. Sci. Technol. B **17** 3168 (1999).

[8]   S.H. Charap, P.L. Lu, and Y. He, IEEE Trans. Magn. **33** 978 (1997)

[9]   C.A. Ross, M. Farhoud, M. Hwang, H.I. Smith, M. Redjdal, F.B. Humphrey, "Micromagnetic behavior of conical ferromagnetic

particles". Submitted to J. Appl. Phys. August, 2000.

[10] F.J. Himpsel, T.A. Jung, P.F. Seidler, "Electronic states in magnetic nanostructures", IBM J. Res. Develop. **42** (1) 33 (1998)

[11] R.K. Nesbet, "Theory of spin-dependent conductivity in GMR materials", IBM J. Res. Develop. **42** (1) 53 (1998)

[12] M.S. Ferreira, J. d'Albequerque e Castro, R.B. Miniz, Murielle Villeret

[13] D. Lammers, A. Cataldo, M. Quan and P. Clarke, "Motorola demonstrates magnetoresistive MRAM". EE Times 113, 1 (2000)

[14] M. Johnson, "Magnetoelectronic memories last and last...". IEEE Spectrum, Feb. 2000, p. 33.

[15] A. Yen, E.H. Anderson, R.A. Ghanbari, M.L. Schattenburg, H.I. Smith, "Achromatic holographic configuration for 100-nm period lithography". Applied Optics **31** 4540 (1992)

[16] A. Yen, M.L. Schattenburg, H.I. Smith, "Proposed Method for fabricating 50-nm period gratings by achromatic interference lithography". Applied Optics **31** 2972 (1992)

[17] H. H. Solak, D. He, W. Li, S. Singh-Glasson, F. Cerrina, B.H. Sohn, X.M. Yang, and N.P. Nealey, "Exposure of 38 nm period grating patterns with interferometric lithography". App. Phys. Lett. **75** 2328 (1999)

[18] Thanks to Maya Farhoud for the use of this figure.

Chapter 2:
Interference Lithography

2.1) Basic Theory

Of all the techniques available for lithographically generating a pattern, the strengths of interference lithography offers an almost ideal match to the needs of patterned magnetic media. Interferometric lithography (IL), allows vast numbers of identical structures to be patterned over a large area with short exposure times and simple equipment. The feature size possible with even mid-ultraviolet wavelengths is beyond what is possible with the most advanced stepper based lithography.

The principle of interference lithography is simple; the interference of coherent light forms a standing wave pattern which can be recorded in photoresist. For two beam interference, the standing wave forms a grating pattern. The mathematical equivalent of this would be Euler's relation, adding together two complex exponentials to get a cosine. The period (*P*) of the standing wave, given in Equation 2.1, is dependent on the wavelength of the light (λ) and the half-angle at which the two beams intersect (θ) [1].

$$P = \frac{\lambda}{2\sin(\theta)}$$

(2.1)
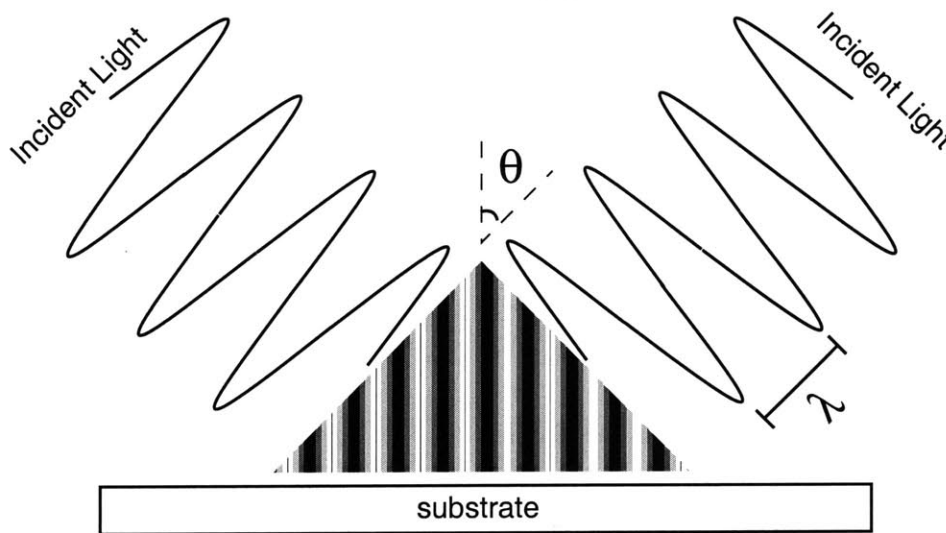
Figure 2.1: *Two-beam interference forms a standing wave.*

A simple schematic is shown in Figure 2.1. Through additional exposures, or the interference of more than two beams, the possible patterns increase from simple gratings to a wide variety of periodic structures. Two-beam interference is by far the most common because of its simplicity, and all applications described in this thesis will be based on two-beam interference. The main limitation of interference lithography is that only periodic patterns can be made. However, in patterned media applications large area periodic patterns are precisely the desired result, so this limitation is of little concern.

2.2) Anti-Reflection Coatings (ARC)

In addition to the primary standing wave formed in the plane of the substrate, there is a second standing wave that can form perpendicular to the substrate. This standing wave is formed by interference between the vertical components of the incident light and light reflected at interfaces in the resist stack. Specifically, when light is reflected at the boundary between the photoresist and the layer underneath, a vertical standing wave forms which can severely degrade the resist profiles (Figure 2.3b). A cartoon of how the incident and reflected light in a photoresist layer forms two perpendicular standing waves is shown in Figure 2.2.
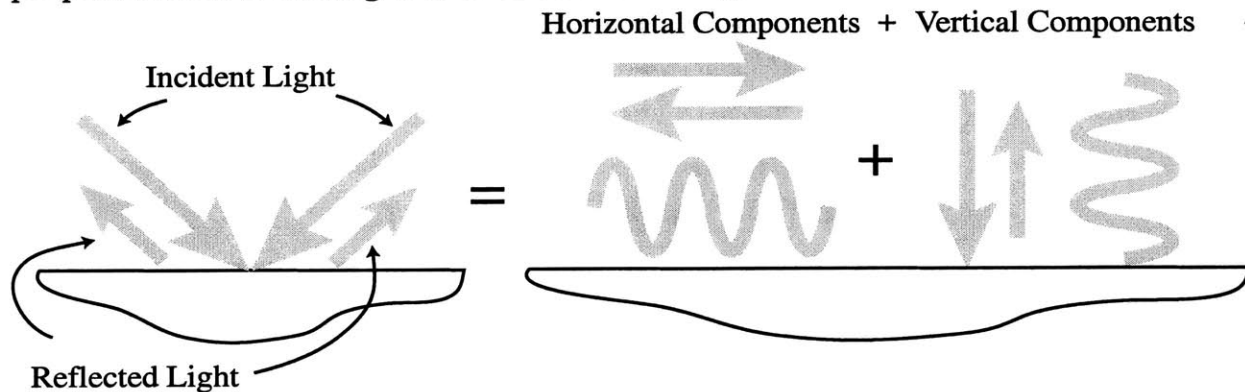
Figure 2.2: *The horizontal and vertical components combine separately to create the desired horizontal standing wave and the undesired vertical standing wave*

The period of the vertical standing wave is determined by the same factors that govern the period of the grating, the wavelength of the light and

the angle of interference. In this case, the refractive index (*n*) of the photoresist also comes into play [1].

$$P_{vertical} = \frac{\lambda}{2n \cdot \cos(\theta)}$$

(2.2)

In addition to a loss of line-width control, the maxima of the vertical standing wave scallop the sidewalls of the resist structure to form a narrow waist. This waist can sufficiently weaken the resist structure so that it topples over during the development process. In a more extreme case, this waist can actually cut through the resist and cause the top section to separate.
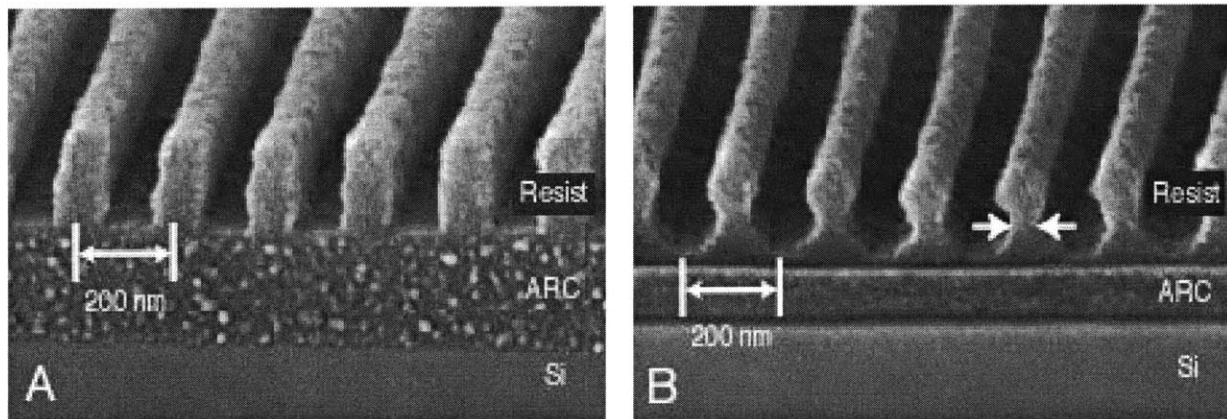
Figure 2.3: *(A) Resist profile of a grating exposed with sufficient suppression of vertical standing wave. (B) Resist profile of a grating exposed with insufficient suppression of the vertical standing wave.*

The severity of the vertical standing wave will vary with the contrast of wave. A higher reflectivity at the resist/substrate boundary leads to a higher contrast standing wave and more damage to the resist pattern. Obviously, one way to decrease the effects of this standing wave is to minimize the reflectivity at this interface. The use of an anti-reflection coating (ARC) underneath the resist is standard procedure for reducing the effects of the vertical standing wave. The photoresist and ARC are often collectively

referred to as the resist stack. An interlayer between the resist and ARC is also sometimes employed to facilitate pattern transfer [2]. In general ARC's work through a combination of absorption and cancellation through interference. Thus, both the thickness and optical constants of an ARC play a role in determining its efficacy.

Figure 2.3a shows a 200 nm pitch grating in 200 nm of positive resist after exposure and development using a 220nm thick layer of ARC. The grating lines have the ideal profile of straight sidewalls and square corners. In contrast, Figure 2.3b shows a 200 nm pitch grating in 200 nm of positive photoresist where the ARC layer is not the proper thickness. The profile of the grating lines shows the effect of the vertical standing wave.

The reflectivity at the resist/ARC interface depends not just on the mismatch in optical indicies between the photoresist and the ARC, but on the optical indicies and thickness of all layers in the resist stack, as well as the angle of incidence. Due to the complexity of the calculations, and the unlimited number of possibilities, a software simulation was developed based on a transmission line model [3] to facilitate the design of effective resist stacks. The program allows the reflectivity at any interface in the resist stack to be calculated for an arbitrary stack design. Although the reflectivity at the lower photoresist interface is usually the primary concern, other interfaces can be of interest in certain situations. For instance, the reflectivity off the top of the resist, the total reflectivity of the entire stack, is an important factor in determining exposure time. Dose calculations will be discussed further in Section 2.3. To enable a proper choice of materials and thicknesses, this program can generate reflectivity curves for variables such as the real or imaginary index of refraction or layer thickness. The permeability of magnetic layers can also affect the reflectivity properties of the stack, so this parameter has been included as well. The permeability is not an intuitive parameter to consider, and is generally overlooked. However, light has both electric (E) and magnetic (H) field components, and high values of permeability will noticeably affect the H field. Other algorithms for calculating reflectivity often ignore the permeability as a contributing factor. The algorithm used in the calculations is described in detail in Appendix A.

Although ARC's have been widely used for a number of years in many forms of optical lithography, there are subtleties to their use that are often overlooked. Two popular misconceptions about ARCs are that their optical

constants should be chosen to match those of the photoresist and that they should be highly absorbent. The truth is that an ARC with either of these properties will probably perform poorly, however there is a basis in truth for both of these assumptions.

The index of refraction can be expressed as the complex quantity *N=n+ik*, where the real term *(n)* accounts for refraction and the imaginagy part *(k)* accounts for absorption. Photoresists most often have very low absorption to allow a uniform exposure throughout the entire thickess of the layer. Therefore their index of refraction is almost entirely real. When discussing index matching to photoresist, it will be assumed that their index is real.

It is true that there will be no reflection at the interface of two semi-infinite layers if the optical constants are matched. The reflection equation in this case is given in Equation 2.3 [4].

$$R = \left(\frac{n_1 - n_2}{n_1 + n_2} \right)^2 \qquad (2.3)$$

In a resist stack the layers must be a finite thickness, and there is always a substrate underneath, so considering the case of semi-infinite layers does not reveal the whole story. Consider an ARC that exactly matches the index of the photoresist. Mathematically there will be no reflection at that interface because there is effectively no interface. The problem in this case is that index matching does not take into account reflections from layers under the ARC. For matched indicies, the ARC and resist are essentially one layer; anything that reflects back into the ARC also affects the resist. For example, consider a single layer of resist over a perfectly reflecting substrate. Obviously light will be reflected back into the resist in this case. Now impose an imaginary boundary somewhere in the resist layer so that it is divided into two sections; the top section is called the resist, and the lower section is called the ARC. Because they are the same material, the resist and ARC are perfectly index matched and there is no reflection at that interface, yet reflections from the mirror surface are not diminished in the upper resist layer.

The popular conception of a highly absorbent ARC is that it will somehow trap the light that comes to it and prevent reflections that way. In

order for this to work, though, light must actually get coupled into the absorbing layer. A materials absorbency (or gain) is described via the imaginary component of the index of refraction, and the real accounts for shortening of the wavelength and hence refraction. If the reflection at the interface of two semi-infinite layers (Equation 2.3) is considered with n_1 and n_2 complex (n_a becomes $n_a\text{-}ik_a$), the equation can be separated to show the individual effect of the real and imaginary components (Equation 2.4).

$$R = \frac{(n_2 - n_1)^2}{(n_2 + n_1)^2 + (k_2 + k_1)^2} + \frac{(k_2 - k_1)^2}{(n_2 + n_1)^2 + (k_2 + k_1)^2} \qquad (2.4)$$

The total reflected power becomes the sum of the reflection due to a mismatch of the real component and the reflection due to a mismatch of the imaginary component. Thus, a highly absorbing ARC can actually be highly reflecting due to the mismatch in the imaginary components of the optical index.

This is not to say that index matched or absorbing ARCs are not sometimes useful, but they are certainly only effective in certain applications. Figures 2.4 and 2.5 show the effect of index matching in two different ARC thickness regimes. The best method for selecting an ARC is based on the processing that will be done after the lithography, rather than its index or absorption properties. As a result, ARCs can be loosely divided into thick and thin regimes. Thin ARC's function more as interference filters than as absorbing layers; there just isn't enough material to make absorption the dominant effect. The self-interference of reflections of the top and bottom surface of the ARC dominates the total reflection back into the resist. In this case, materials ranging from partially absorbing to non-absorbing can be used to subdue reflections. Highly absorbing materials can be used in this case despite the fact that interference effects from the secondary surface reflections are muted. The large mismatch in indicies caused by the high absorbance can null reflections into the resist with very thin ARC films. Similarly, non-absorbing ARC's with a large mismatch in the real index can accomplish the same thing. Non-absorbing dielectric ARC's have been well studied, and are not the focus of our attention. The necessity of a thin ARC layer, or the chemical characteristics necessary for

pattern transfer drive the selection of an ARC material rather than the optical characteristics in the thin ARC regime. Figure 2.5 shows the reflectivity curves at the resist/ARC boundary for a highly reflecting aluminum surface. The hypothetical ARC in this example has a 75 nm film thickness. The real and complex components of the index of refraction are varied independently in 2.5a and 2.5b. In 2.5a, the real part of the index is matched to the photoresist, at *n=1.79*, while the absorption coefficient is varied from highly absorbing (*k=-1*) to non-absorbing (*k=0*). The reflectivity at k=0, where it is perfectly index matched to the photoresist, is seen to be very high due to the high reflectivity of the aluminum substrate. The null is found at a moderate absorbance of *k=-0.4*, and increases for more absorbing films. If the null level of *k=-0.4* is assumed as constant and the real index varied, as seen in Figure 2.5b, then it is observed that the reflectivity null occurs not at the matched index of *n=1.79*, but at a lower value around *n=1.45*. This concrete example shows that in the thin ARC regime, that both a fairly high absorbance as well as a difference in real index may be necessary to optimally reduce back reflections.

On the other hand, thick ARCs are more likely to have absorption effects dominate over interference as seen in Fig. 2.4. In this case, the secondary reflections off the lower surface of the ARC are muted out, and the reflection into the resist is primarily determined by the index mismatch. A thick ARC with a high absorption coefficient will eliminate substrate reflections more rapidly, but the back reflections off the ARC itself will be high. For this reason, the absorption of a thick ARC must be quite low, even though absorption is relied on to reduce substrate reflections. A thick ARC can be useful for fully isolating the resist layer from topographical variations on the substrate, or if a tall template is desired for applications such as electroplating [3]. In this regime, the thickness of the ARC is unimportant as long as it exceeds a certain value, and the reflection from layers underneath the ARC do not affect the resist at all. Figure 2.4 shows an example resist stack with a 200 nm thick resist over a 750 nm thick ARC layer on a highly reflecting aluminum substrate. Figure 2.4a shows the reflectivity at the resist/ARC boundary for variations in the absorbance of the ARC and a real index fixed at 1.79 to match the photresist. As in Figure 2.5a, the reflectivity for *k=0* is very high, but drops off extremely rapidly to a minimum at around *k=-0.1*. This absorbance value is much lower than in the

thin ARC regime depicted in Figure 2.5a. In Figure 2.4b, we see that the minimum in reflectivity is found when the real index of the ARC is matched to that of the resist, n=1.8. The two plots in Figure 2.4 show that index matching with a low absorbance will optimally reduce reflections. It is important to note that in both the thick and thin regimes, a perfect index match between the ARC and the resist led to *maximum* reflectivity.
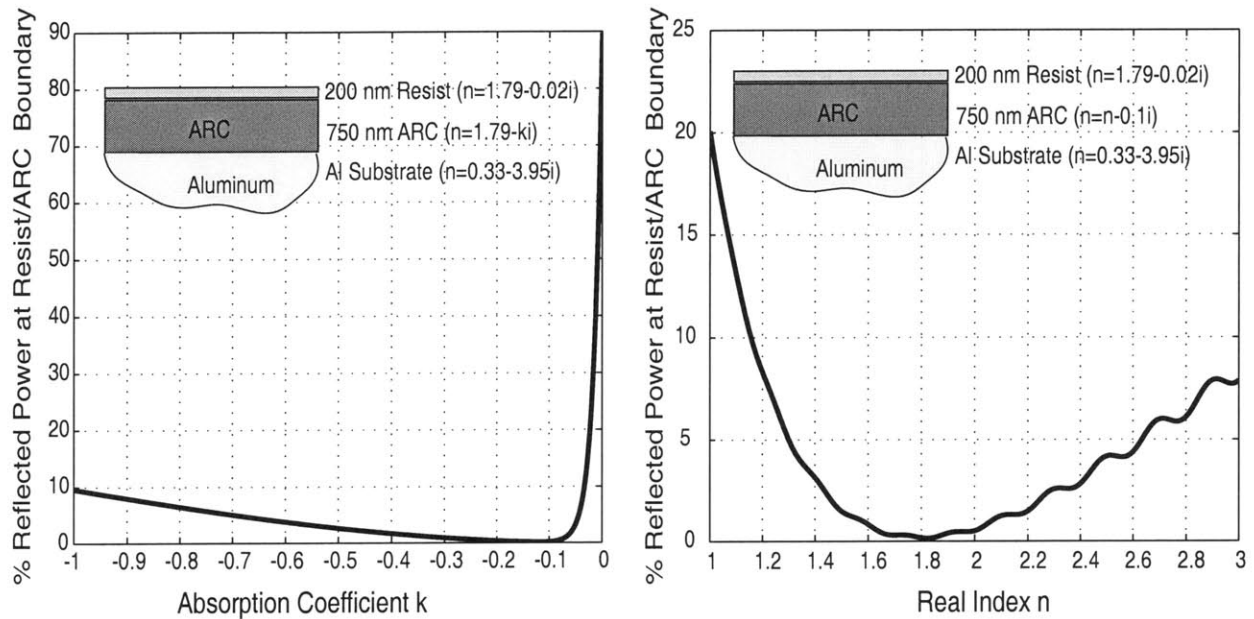
**Figure 2.4:** *Index Matching in the thick ARC regime*
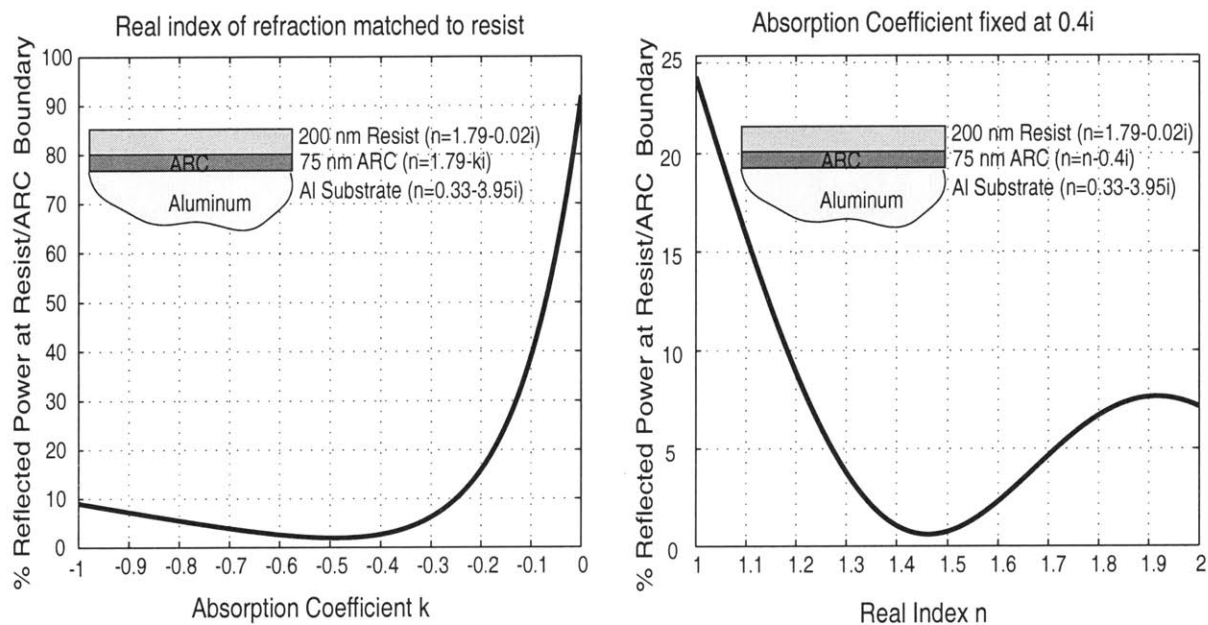
Figure 2.5: *Index matching in the thin ARC regime.*

2.3) **Photoresist Contrast and Dose**

The reason ARC's are used is to suppress secondary reflections, and enable a good profile in the photoresist. However, obtaining a favorable resist profile also requires consideration of the exposure dose and contrast of the interference fringes. The exposure dose in often measured by multiplying the intensity of the incident light by the time of the exposure, yielding a value in energy per unit area. In interference lithography, a dose calculated in this manner is only valid for the specific conditions of that exposure. If the dose is used for a different period grating, or in a different resist stack, the results will be unpredictable. It stands to reason that a resist film of a given thickness must have the same exposure dose for all conditions. To obtain a dose which is valid for any period grating on any substrate, a more detailed calculation must be done.

The dose as described so far is not the dose that the resist experiences, only the dose that is incident on the substrate. For this reason, I will refer to it as the incident dose (D_i). This incident dose is generally much higher than the actual exposure dose of the resist. There are three parameters which serve to determine the actual dose experienced by the resist. They are the angle of incidence of the light, the reflectivity of the top surface of the resist, and the reflectivity of the bottom surface of the resist.

The angle of incidence of the light serves to reduce the apparent intensity of the beam through a simple cosine relation. As the angle moves off normal, the cross-section of the substrate in the beam decreases, but the area of the substrate remains the same. Thus, less light is used to expose the same area, and the effective intensity is reduced.

The angle of incidence θ also plays an indirect role in determining the reflectivity from the front and back surfaces of the resist. The front surface reflectivity (R_f) determines how much of the incident power is coupled into the resist, and how much is lost immediately to reflection. This number I call the coupling efficiency (e_c), which is defined $e_c=1-R_f$. A low reflectivity at the top surface of the resist will reduce exposure times. Similarly, the reflectivity at the back surface of the resist (R_s) is equivalent to having an additional beam incident from the back, which also serves to reduce exposure times. When a properly designed ARC is used, the secondary

surface reflectivity is close to zero and can be ignored. However, Chapter 5 will discuss resist stacks which have high back surface reflectivity; in this case the dose correction is important. If we combine all of these factors, we can get an equation which can be used to convert the incident dose to the equivalent exposure dose (D_E).

$$D_E = D_I \cdot e_c \cdot (1 + R_s) \cdot \cos(\theta) \qquad (2.5)$$

For an empirically determined incident dose under one set of conditions, the equivalent dose found with this calculation can be applied to any substrate at any period grating. The incident angle is related to the period of the grating by Equation 2.1, and the reflectivity values for the front and back resist surfaces can be found using the simulation described in Section 2.2 and Appendix A. The one factor which is not accounted for in this equation is resist thickness. The volume of resist will affect the exposure dose in a non-linear way, but this has not been thoroughly examined.

For a known equivalent dose at a given resist thickness, the incident dose necessary for a different period or substrate can be found by solving Equation 2.5 for D_I.

$$D_I = \frac{D_E}{e_c \cdot (1 + R_s) \cdot \cos(\theta)} \qquad (2.6)$$

Another aspect of the resist which should be considered is how it responds to the contrast of the interference fringes. Section 3.4 will discuss the effects of source bandwidth and interferometer design on fringe contrast. Right now, however, we will examine the effects of fringe contrast on the resist.

In the situation of perfect contrast, the intensity peaks have their highest value and the nulls are exactly zero. When contrast decreases, the minima of the interference pattern increase from zero, and the maxima decrease. In a lithographic exposure this means that the areas of resist which should be exposed and developed away may not be fully cleared, and the areas of the pattern which should remain intact will be exposed and begin to wash out. Fringe contrast must be above a certain level in order to get a good exposure. A better resist will be able to tolerate lower contrast in the fringes.
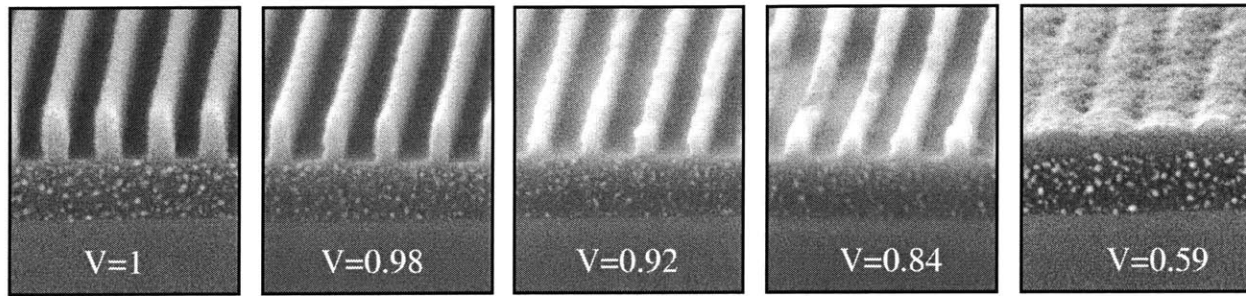
Figure 2.6: *Degradation of resist profiles for low contrast exposures*

In order to determine how the resist responds to lowered fringe contrast, we can examine how the profiles deteriorate away from the center of a wide-area exposure. Details of the path length and fringe contrast calculations can be found in Chapter 3. Figure 2.6 shows a series of 200 nm period gratings exposed with interference lithography where the fringe contrast is varied. Fringe contrast, or visibility (V) is discussed in greater detail in Ch.3, and defined in Equation 3.2. For very high fringe visibility, $V=1$ and $V=0.98$, the resist profiles look fine. At a lower contrast of $V=0.92$, the profiles are more ragged and significantly thinner due to the higher dark-area exposure. For contrast of 0.84, the profiles are quite poor, and the exposure is lost at a contrast of 0.59. If we consider a fringe contrast of 0.9 as the cutoff for acceptable resist profiles, the maximum area over which an acceptable exposure will occur can be determined. This is explored in Chapter 3.

2.4) Dots and Ellipses

So far the discussion of interference lithography has centered around printing gratings, but for patterned magnetic media we are primarily interested in arrays of discrete elements. Prior work has shown that printing a square grid of circular features is possible [6-13]. The simplest method is exposing a grating at approximately 60% dose, rotating the sample by 90 degrees, and exposing another grating at 60% dose. The two consecutive exposures combine to produce a grid. Using a more complex interferometer, grids can also be printed using the interference of more than two beams. It has been shown that multiple beam interference can produce higher contrast images, but due to the increased complexity of the equipment, this approach is rarely used [9].

To store a binary bit of information, a magnetic particle must have a single easy axis of magnetization. This restricts the magnetization states to pointing either up or down along that axis. When a grid of circular structures is patterned, the only option for creating a shape anisotropy is in the vertical direction; i.e. make the structure taller than it is wide. Arrays of structures with out-of-plane anisotropy, such as evaporated [11-15] or electroplated [10,16,17] pillars, have been fabricated and studied extensively. Another option would be to use films that had anisotropy due to their crystalline microstructure.

in-plane shape anisotropy   out-of-plane shape anisotropy
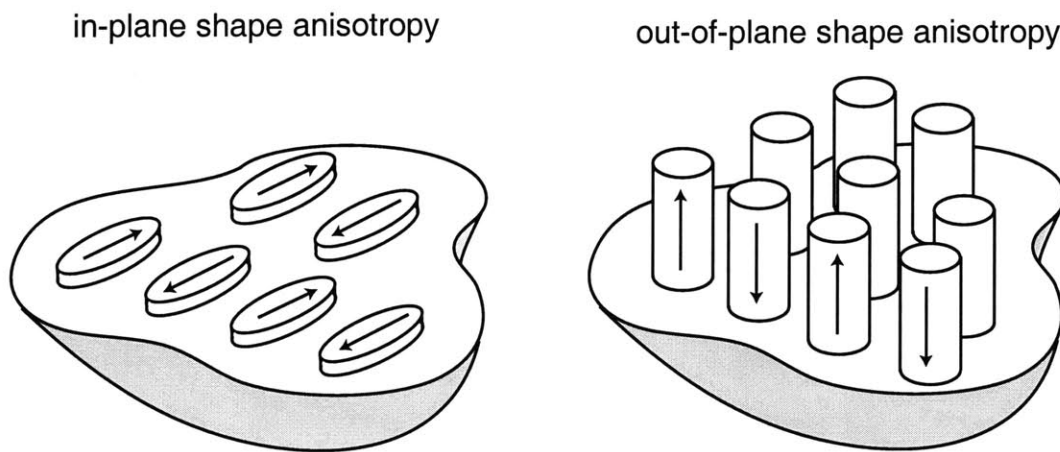
Figure 2.7: *Arrays of magnetic structures with in-plane and out-of-plane shape anisotropy. The arrows indicate axes of preferred magnetization.*

Figure 2.7 depicts particles with in-plane and out-of-plane shape anisotropy. Although the areal density of magnetic particles with out-of-plane shape anisotropy is potentially higher than that possible with in-plane features, there are a number of reasons why in-plane shape anisotropy is desirable. In-plane features, for example, are more amenable to reading and writing with the current design of read-write heads. Also, read and write schemes proposed for MRAM devices benefit from in-plane anisotropy. Finally, the switching behavior of in-plane particles in comparison to out-of-plane particles is of interest in the development of micromagnetic theory [17,18].

Same Dose

60% x 60 %

Same Period
200 nm x 200 nm

(A)

100 nm

100 nm

Same Dose

60% x 60 %

Dual Period
200 nm x 1000 nm

(B)

1000 nm

Dual Dose

100% x 60 %

(C)

100 nm

600 nm
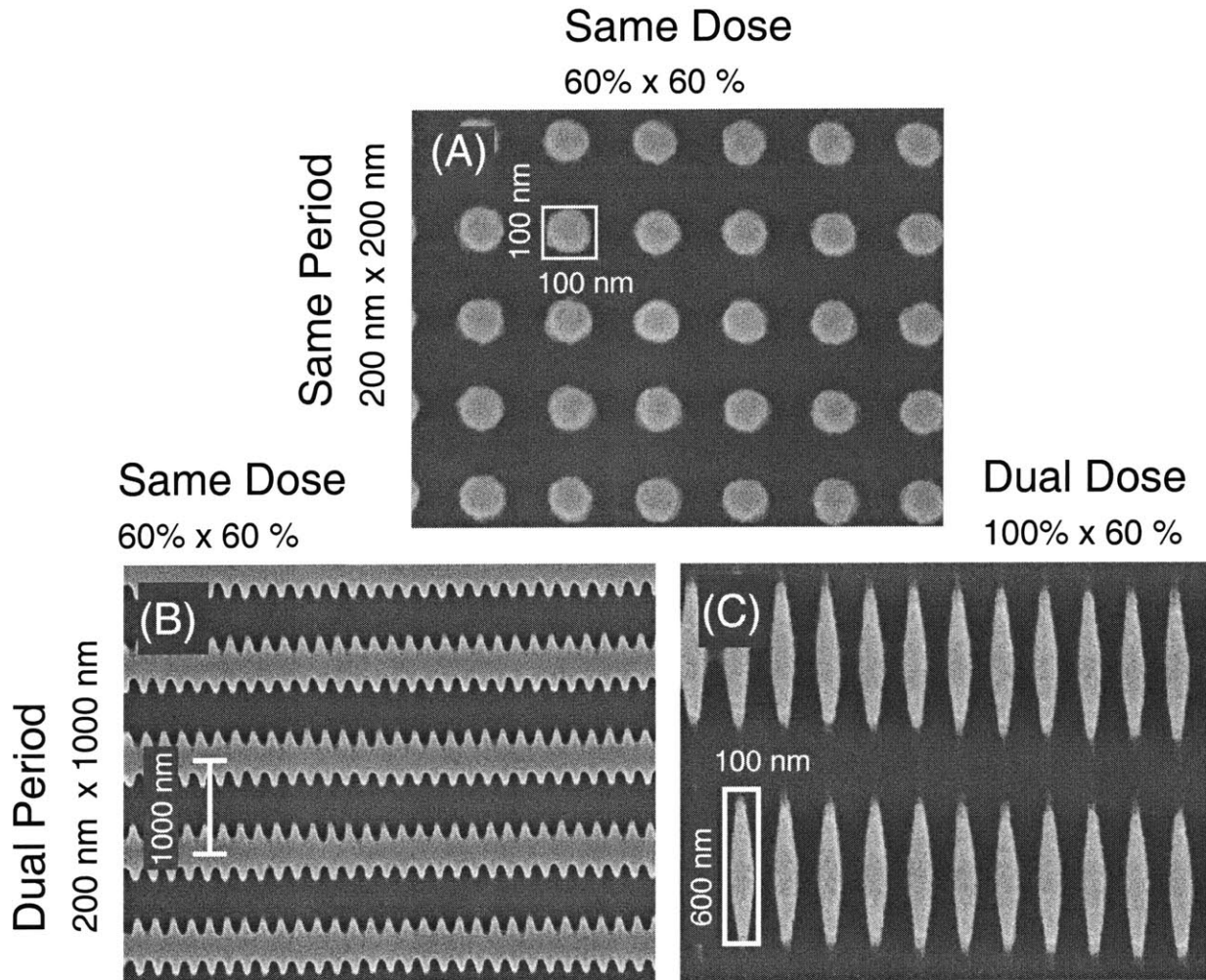
Figure 2.8: *Arrays of resist structures illustrating the dual-dose and dual-period techniques for printing ellipses. The dose is normalized to percentage of a clearing dose for a grating of the same period.*

To create an in-plane shape anisotropy, the magnetic elements must become either elliptical or rectangular in shape. Fabrication of magnetic nanostructures with in-plane anisotropy requires some modification of the IL exposure. Using a two-beam IL system, three possible methods of patterning arrays of anisotropically-shaped features are possible. As in printing circular dots, ellipses are made by overlapping two grating exposures. Patterning arrays of circular dots can be thought of a special case of any of the methods for patterning ellipses. Any or all of these techniques can be used in combination to increase control over the array parameters, but for clarity

they will be discussed individually. The discussion will be limited to patterning dots in positive resist, although the same methods will apply to patterning holes in negative resist.

The first method relies on using a different dose in the first and second grating exposures. To make a complete exposure, the lower of the two doses can only be as low as the clearing dose for circular dots. The higher of the two doses is an overexposure which thins the dot in one direction. In this case, the dimensions and area of the elliptical feature will always be smaller than a circular dot printed with the same pitch grating. Overexposing the dot in one direction causes the feature to shrink in both directions, and often the result is circular. The maximum dose is limited by what will cause the entire pattern to develop away. The range of aspect ratio's possible with this approach is limited to less than about 2:1.

The second method uses orthogonal exposures of two different periods. Although this method can be difficult to implement using conventional IL systems, the Lloyd's-mirror interferometer described in Ch. 3 allows this to be done easily. The interferometers used for this work are capable of producing gratings with spatial periods having a practical range from ~175 nm to many microns. Because of the large range of periods, this method allows a greater range of possible aspect ratios than the other two, with ratios up to at least 10:1 being possible. Exposing high aspect ratios with the dual-period method means that the spacing along the short axis becomes much smaller than the spacing along the long axis, as seen in Fig. 2.8c. Magnetic particles in a lattice of this sort would encourage alternating magnetization of neighboring elements, and only minor interactions would occur between the long-period rows.

Figure 2.8b shows high-aspect ratio dots exposed using a 200 nm period grating orthogonal to a 1000 nm period grating with equal equivalent doses in each exposure. Equations 2.5 and 2.6 were used to ensure that the equivalent dose in each exposure was equal. It is clear in this case that the dots are not fully exposed in the short-period direction, the result is a 1000 nm period grating with modulations in the grating wall. Figure 2.8c shows a combination of the dual-period and dual-dose techniques where 200 nm period exposure was given a full grating dose, and the 1000 nm period exposure was given a 60% grating dose. The result in this case is the

expected result for the previous case. High-aspect ratio ellipses are formed with close packing along the short-period direction and wide spacing in the long-period direction. Although not shown, a series of exposures were done with intermediate doses in the short period direction. It was found that a full grating dose was necessary in order to fully clear the resist. This is a very curious result, and one which explicitly displays the non-linear nature of resists. The most plausible explanation for this behavior is a proximity effect.

200 nm x 200 nm   **200 nm x 1000 nm**

2000 nm

High Intensity   Saddle Point   Low Intensity
(Develops Away)   (Causes problems)   (Resist Structure)
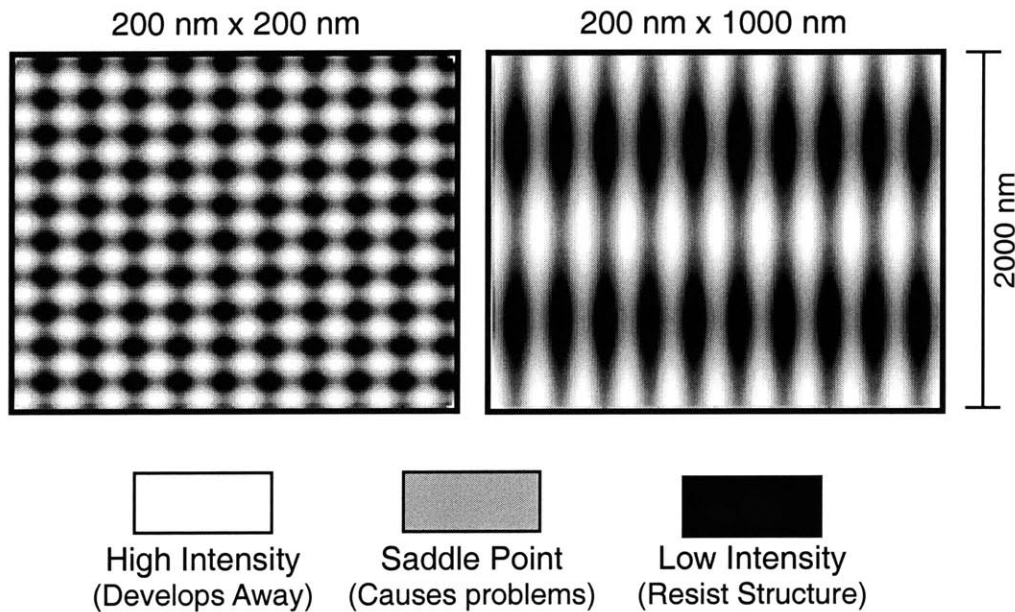
Figure 2.9: *Intensity distributions in the exposure of 200nm x 200nm and 200nm x1000nm grids. The proximity of dark area saddle points to high intensity nodes determines the exposure characteristics.*

Consideration of the lateral intensity profiles for a single-period grid and a dual-period grid may help to illuminate the nature of the disparity. Figure 2.9 shows simulated intensity profiles for the two different cases seen in Figure2.8 a,b. The intensity, or dose, can be spilt up into 3 ideal regions: high intensity nodes, saddle points, and low intensity nodes. The high intensity nodes occur at the overlap of the two individual gratings and give at least a full clearing dose. The saddle points have only half this dose and the low intensity nodes give no dose. In a positive resist, the low intensity nodes form the desired resist structures, but only if both the high intensity

nodes *and* the saddle points clear. For the circular dots shown in Fig 2.8a, the saddle points have only 60% of the required clearing dose, but they clear anyway. This surprising effect must be due to the close proximity of the high intensity nodes increasing the development rate of the saddle points.

In Figure 2.8b,c, it was clear that the saddle points do not fully develop until a full clearing dose is provided. In Figure 2.9b, the saddle points which run through the dark area of the 1000 nm period grating are the ones which need to clear before the ellipses fully separate from one another. The high intensity nodes are much further away in this case, which eliminates the proximity effect that was necessary to develop these regions at a lower dose. Thus, complete exposure of the short period grating is decoupled from the exposure of the large period grating, and a full grating dose is needed. Notice that the reverse of this is not true, the exposure of the large period grating, which can still be done with ~60% of the grating dose, is not decoupled from the exposure of the small period grating. It is expected that for dual-period exposures where the spatial periods of the two gratings are closer that there will be some intermediate state in which the exposure dose of the short-period grating is larger than 60%, but not yet 100% of the full grating dose although verification of this has not been pursued as part of this thesis.

The third method uses two off-orthogonal exposures of equal-period gratings to modify the dimensions of the exposed features. Where circular features use two consecutive exposures at 90° to one another, an ellipse will be formed when the exposures are done at any other angle. The features will be long and narrow if the angle between the exposures is small, and will approach circular as the angle approaches 90°. This method is capable of making arrays of high aspect ratio features which are closely packed. At high aspect ratios, the features become longer and the space between them in the long direction diminishes. Features become farther apart along the short axis than the long axis, which is complimentary to the dual-period grid where features are widely spaced along their long axis. In the limit of zero angle between the exposures, they would all line up and form a grating. For this reason, the magneto-static interaction of the particles along their principal axis increases with aspect ratio. This can be either a boon or a hindrance, depending on the intended use of the particles. It is also interesting to note that the exposure dose required using this method is the same as that

required for printing circular dots, about 60% of the clearing dose of a grating. This is to be expected, because there is no change in the periodicity of the exposure gratings to reduce proximity effects. Figure 2.10 shows two arrays of structures in resist with different aspect ratios. The high aspect ratio structures seen in Fig. 2.10a, exposed by 200 nm period gratings at intersecting at ~20°, are seen to be closely spaced in the long direction. Figure 2.10b shows dots exposed using a 70° angle between exposures. These structures are much closer to circular, with an aspect ratio of only 1.4.
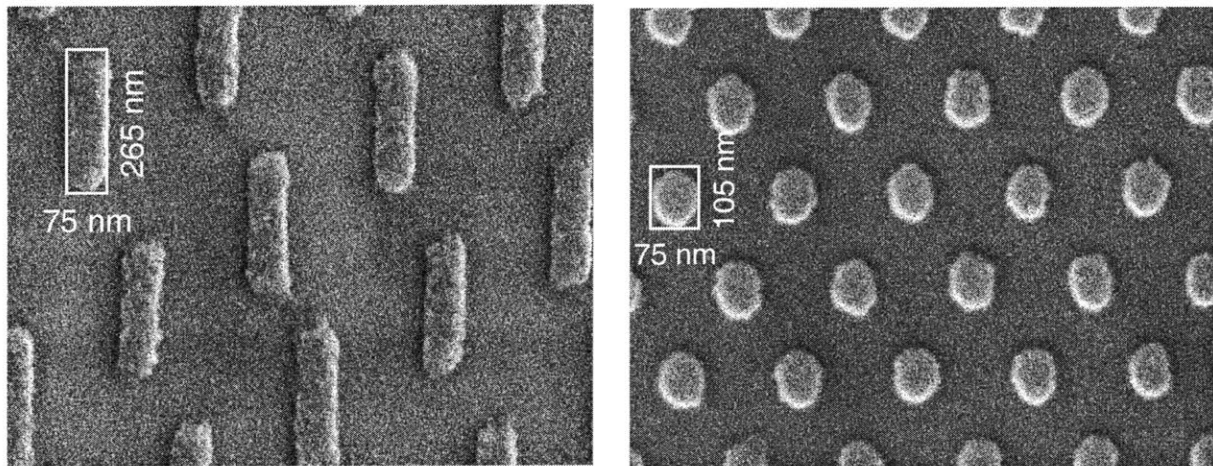
Figure 2.10: *Arrays of resist structures printed with an off-orthogonal grid exposure: (A) exposure angle 25° from first grating with an aspect ratio of 3.5, (B) exposure angle 70° from first grating for aspect ratio of 1.4.*

Comparing the advantages and disadvantages of these three methods for exposing ellipses using IL, the use of off-orthogonal grids seems to be the most practical for low to medium-high aspect ratio features. The exposure dose is independent of aspect ratio, and easily determined from the grating dose at that period. The reflectivity properties of the resist stack will be the same for both half-exposures, so standing wave effects are not a concern as in the dual-period method. Because resist stacks are designed to be used for one period, the reflectivity properties will be less than ideal at other periods. The reflectivity at the near-normal incidence angles needed for long-period gratings can be significantly different from the reflectivity at the near-grazing angles used to print short-period gratings. Thus, standing wave problems

will usually be apparent in at least one of the exposures of a dual-period grid. Also, the additional work of physically modifying the interferometer between exposures to print a different period is avoided when using the off-orthogonal method. However, for very high aspect ratio ellipses beyond what is possible using off-orthogonal exposures the dual-period method must be used. In this case, the exposure of the short period grating will require a full grating dose, while the exposure of the long period grating will require only ~60% of a grating dose.

2.5) References

[1] H.I. Smith, <u>Submicron- and Nanometer-Structures Technology</u>. NanoStructures Press Sudbury, MA. 1994

[2] M.L. Schattenburg, R.J. Aucoin, and R.C. Fleming, "Optically Matched trilevel resist process for nanostructure fabrication", J. Vac. Sci. Technol. B **13** 3007 (1995)

[3] S. Ramo, J.R. Whinnery, T. van Duzer, <u>Fields and Waves in Communication Electronics</u>. Wiley, New York, 1994

[4] E. Hecht, <u>Optics</u>, Addison Wesley, Reading MA 1987

[5] C.A. Ross, H.I. Smith, T.A. Savas, M.L. Schattenburg, M.Farhoud, M. Hwang, M. Walsh, M.C. Abraham, R.J. Ram, "Fabrication of patterned media for high density magnetic storage" J. Vac. Sci. Technol. B, **17** 3168 (1999)

[6] M. Farhoud, J. Fererra, A.J. Lochtefeld, T.E. Murphy, M. L. Schattenburg, J. Carter, C.A. Ross and H.I. Smith, " Fabrication of 200 nm period nanomagnet arrays using interference lithography and a negative resist". J. Vac. Sci. Technol. B, **17** 3182 (1999)

[7] J.Y. Decker, A. Fenrandez, D.W. Sweeney, "Generation of subquarter-micron resist structures using optical interference lithography and image reversal". J. Vac. Sci. Technol B **15** 1949 (1997)

[8] T.A. Savas, S.N. Shah, M.L. Schattenburg, J.M. Carter, H.I. Smith, "Achromatic interferometric lithography for 100-nm-period gratings and grids". J. Vac. Sci. Technol. B **13** 2732 (1995)

[9] A. Fernandez, J.Y. Decker, S.M. Herman, D.W. Phillion, S.W. Sweeney and D.M. Perry, "Methods for fabricating arrays of holes for interference lithography", J. Vac. Sci. Technol. B, **15** 2349 (1997)

[10] M. Farhoud, M. Hwang, H.I. Smith, M.L. Schattenburg, J.M. Bae, K. Youcef-Toumi, C.A. Ross, "Fabrication of Large Area Nanostructured Magnets by Interferometric Lithography" IEEE Trans. Magn. **34** (4) 1087 (1998)

[11] M Thielen, S. Kirsch, H. Weinforth, A. Carl, E.F. Wasserman, "Magnetization reversal in nanostructured Co/Pt multilayer dots and films". IEEE Trans. Magn. **34** (4) 1009 (1998)

[12] E.F. Wasserman, M. Thielen, s. Kirsch, A. Pollman, H. Weinforth, and A. Carl, "Fabrication of large scale periodic magnetic nanostructures". J. Appl. Phys. **83** (3) 1 (1998)

[13] M.A.M Haast, J.R. Schuurhuis, L.abelman, J.C. Lodder, Th.J. Popma, "Reversal mechanism of submicron patterned CoNi/Pt multilayers". IEEE Trans. Magn. **34** (4) 1006 (1998)

[14] T. Ono, H. Miyajima, K. Shigeto, T. Shinjo, "Dot-arrays of Co/Pt multilayers with perpendicular magnetic anisotropy". J. Magn. and Mag. Mat. **198** 225 (1999)

[15] S.Y. Chou, M.S. Wei, P.R. Krauss, P.B. Fischer, "Single Domain magnetic pillar array of 35 nm diameter and 65 Gbit/in.^{2} density for ultrahigh density quantum magnetic storage", J. Appl. Phys. **76** (10) 6673 (1994)

[16] J. Wong, A. Scherer, M. Todorovic and S. Schultz, "Fabrication and characterization of high aspect ratio perpendicular patterned information storage media in an Al_2O_3/GaAs substrate". J. Appl. Phys. **85** (8) 5489 (1999)

[17] M. Hwang, M. Farhoud, Y. Hao, M. Walsh, T.A. Savas, H.I Smith, C.A. Ross, "Major Hysterisis Loop Modeling of Two-dimensional Arrays of Single Domain Particles" Submitted for publication in IEEE Trans Magn. September 2000

[18] R.P. Cowburn and M.E. Welland, "Analytical micromagnetics of near single domain particles". J. Appl. Phys. **86** (2) 1035 (1999)

Chapter 3:
The Lloyd's-Mirror Interferometer

3.1) IL at the Space Microstructures Laboratory

Two different interferometers were used for the lithography described in this thesis. Although both interferometers print gratings using two-beam interference, the implementation is very different. The first interferometer, located in the Space Microstructures Laboratory (SML) at MIT, is a design that has been used and studied extensively [1-4]. The architecture of the interferometer is shown in Figure 3.1. The source is a 1 watt argon ion laser with a wavelength of 351.1 nm. The beam is split into two arms, and each arm contains a spatial filter and beam expansion assembly. The spatial filters are used to eliminate noise from the beam which would otherwise be printed as distortion in the grating. The beam expansion takes place over about 1 meter from the spatial filter to the exposure plane. In addition to giving a greater exposed area, expansion allows the beam to be approximated as a spherical wave, and the large radius of the spherical wave allows a plane wave approximation over small areas.
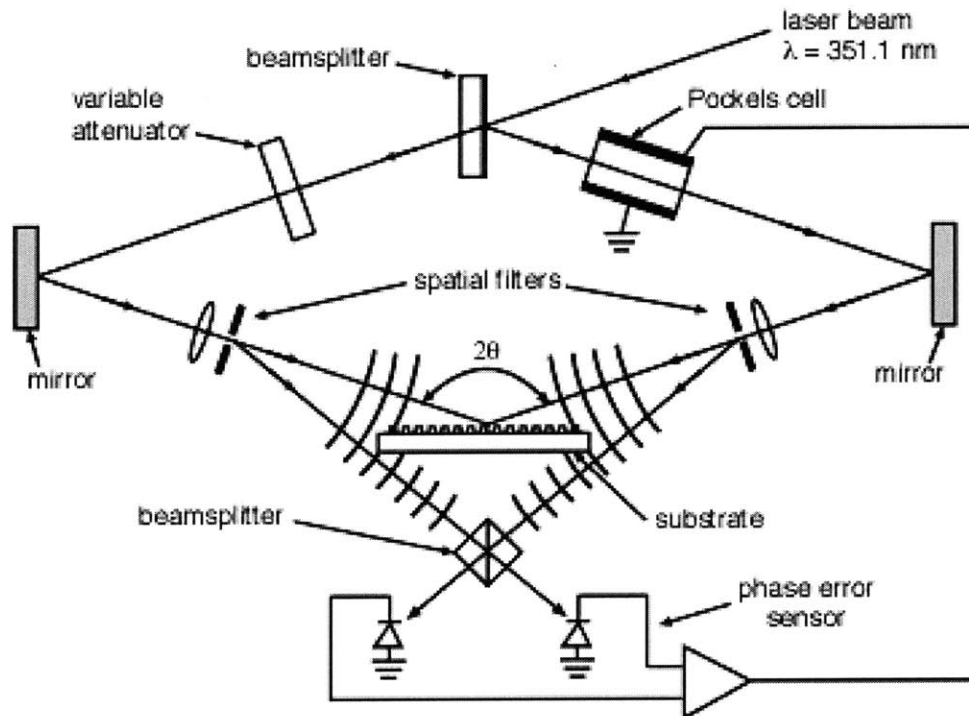

Figure 3.1: *The interference lithography system in the SML.*

The effect of a small optical path length difference is to reduce the visibility of the interference fringes. Ideally the two arms of the interferometer will be equal in length, however a small change in path length is negligible as long as the difference is constant. Much more damaging is a changing path length in one or both of the arms, which causes the placement of the interference fringes to drift. Even a fraction of a wavelength variation in the length of the two arms can ruin an exposure. The length of each arm of the interferometer is roughly two meters, and each arm contains numerous optical elements. Thus, even such minor disturbances such as air currents can cause noticeable variations in an exposure. A Pockels cell in one of the arms, part of a feedback system, is used to compensate for these dynamic phase variations, and is described elsewhere [1,3].

The primary function of the IL system in the SML is as a production tool for high quality x-ray optics used in satellite instrumentation. The exacting nature of this work requires that very little modification and experimentation be done with this apparatus. To circumvent this problem, a new interferometer was designed and built as part of this thesis to facilitate work not only in patterned magnetic media, but in other applications such as field-emission displays and integrated optics.

3.2) Lloyd's-Mirror Interferometer

A variety of methods exist for the separation and recombination of a beam to produce interference fringes. One method, proposed by Lloyd in 1837 [5], involves using a broad beam of light and a mirror to fold a portion of the wavefront back onto itself. Figure 3.2 shows a schematic of the Lloyd's mirror interferometer. Although Lloyd's' initial concept, and more recent implementations [6], used the angle of the mirror in relation to the image plane to set the angle of interference, I have modified the design slightly and fixed the mirror perpendicular to the image plane. The image plane in this interferometer is the substrate to be patterned, and the interference fringes are recorded in the resist. With the mirror rigidly fixed perpendicular to the surface, the angle of interference, and thus the period of the grating, is set by rotating the mirror/substrate assembly around the point of intersection of the mirror and the substrate. Like the SML style interferometer, the period of the grating is given in Equation2.1. Although the light is incident on the substrate at a different angle than the mirror, simple trigonometry guarantees that the light reflected off the mirror is always incident on the

substrate at the same angle θ as the original beam. By having the mirror at a fixed angle to the substrate, the mirror can be brought into physical contact with the substrate to reduce scattering noise. In a design with the mirror angle variable, there will always be a gap between the mirror and the substrate.
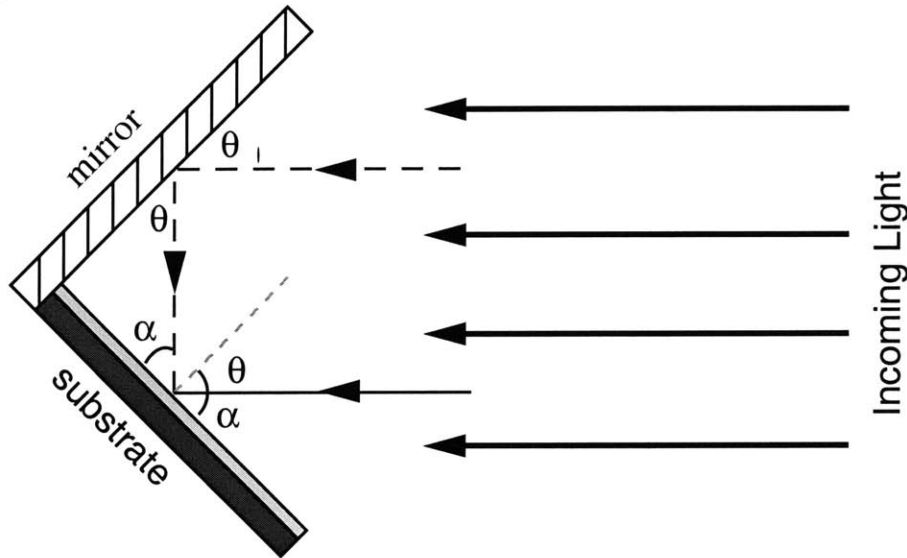
Figure 3.2) *Basic Lloyd's mirror configuration*

Rather than being a direct replacement for the SML style interferometer, the Lloyd's mirror fills a complementary role. While the SML system is very sensitive to vibrations, beam motion, and other factors, the Lloyd's mirror is almost immune to these effects. The physical separation of the two beams into two arms in the SML system gives rise to this sensitivity. In the Lloyd's mirror, a single beam is used for most of the optical path. Only in the last few centimeters, when a portion of the beam reflects off the mirror, does the beam split into two. A rigid mechanical connection between the mirror and the substrate means that the relative lengths of the two arms is very stable. Variations in the path length of one arm relative to the other only occur if the mirror moves in relation to the substrate. Because the mirror is fixed in relation to the substrate, vibrations of the assembly or wandering of the incoming beam do not affect the exposure. This negates the need for a phase locking system, a mandatory component of the SML interferometer. Where precise alignment and continual adjustment to maintain this alignment are necessary in the SML style interferometer, the Lloyd's mirror requires minimal alignment and adjustment.

Another advantage of the Lloyd's mirror interferometer is the simplicity with which the period of the grating can be changed. As mentioned earlier,

this requires only a rotation of the mirror/substrate assembly. Realignment or repositioning of components is unnecessary. In the SML system, the optics for each arm must be moved and realigned, a process which can take many hours.

However, the simplicity and robust nature of the Lloyd's mirror can come at the expense of grating fidelity. In the SML style interferometer, the last optical element that the beams encounter before they interfere is the spatial filter. The state of the beam by the time it propagates over 1 meter to the exposure plane is such that the true Gaussian profile of the beam can be accurately approximated by a spherical wave. The interference of two spherical beams can be analytically calculated, and the distortion from a linear grating characterized [7]. Additional noise from imperfect optics or scattering is eliminated from the beam by the spatial filter. This is not so in the Lloyd's mirror, where a number of factors can limit the linearity of the gratings. Of primary concern is the addition of a mirror to the optical path after the spatial filter. The flatness of the mirror directly affects the grating quality, although this problem can be reduced significantly with a high quality mirror. Phase variations introduced by a mirror which is not perfectly flat will cause the grating to distort. For the same reason, the Lloyd's mirror system is also more sensitive to dust particles than the SML style interferometer. Scattering from dust particles or scratches on the mirror act as point sources of coherent noise and can severely compromise grating linearity. Another concern with the Lloyd's mirror is that the intensity of the two arms will never be equal, thus reducing the contrast of the interference fringes. This topic will be discussed further in Section 3.4. The SML interferometer has the capability to adjust the power in each arm independently, allowing the two arms to be equalized.
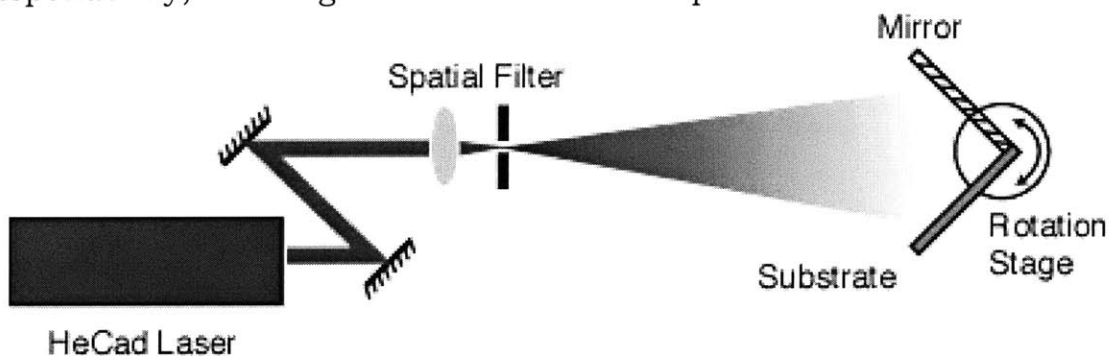

Figure 3.3: *A cartoon of the Lloyd's Mirror interference lithography system.*

3.3) Implementation of Lloyd's Mirror Lithography

A cartoon of the Lloyd's mirror interferometer as implemented for lithography is shown in Figure 3.3. A 54 mW helium cadmium laser emitting a single TEM 00 mode at 325 nm is used as the source. The HeCd offers a long (30 cm) coherence length at a mid UV wavelength in a more robust package and at a lower cost than other options, such as argon-ion or excimer lasers. A pair of mirrors directs the beam from the laser head to the spatial filter, and allows for alignments with the center of the wafer stage. The spatial filter allows high frequency noise to be removed from the beam to provide a clean Gaussian profile. After the spatial filter, the beam is allowed to expand over 1.73 meters. The large beam expansion in the Lloyd's mirror is somewhat of a tradeoff, but in this case, more is gained than is lost. As a Gaussian beam expands, it changes in three ways. The intensity of the beam decreases, the diameter of the beam increases, and the radius of the phase front increases. Lowering the intensity leads to increased exposure times, but the inherent stability of the system means that this is of little consequence to the patient experimenter. A typical exposure time is on the order of ten minutes with this system, while the SML interferometer has exposure times typically less than a minute. Because of the Gaussian intensity profile, increasing the beam diameter means that the intensity will be more uniform over the exposed area. Finally, the increase in radius of the beam diameter means that the beam more closely approximates a plane wave over the exposure area. Consequences of this are explored in Section 3.4. After the expansion over 1.73 meters, the beam diameter is 36 cm and the phase front can be accurately described as spherical with a radius of curvature 1.7 meters.

A 5 inch square mirror is used to minimize the effects of edge scattering seen in the exposure. The mirror is made of aluminum because of its enhanced UV reflectivity compared to other metals, and for its essentially constant reflectivity over a broad range of angles. A higher reflectivity can be obtained with a dielectric mirror, but the variation in reflectivity with angle can be significant. The intersection point of the mirror and wafer is aligned with the axis of a rotation stage, this allows for easy variation of the gratings' spatial period. Because the center of the mirror/substrate assembly remains on the optical axis, further alignment of the optics is unnecessary. This feature is a distinct advantage over the SML style system,

where changing the period requires physically moving and re-aligning the two arms of the interferometer.
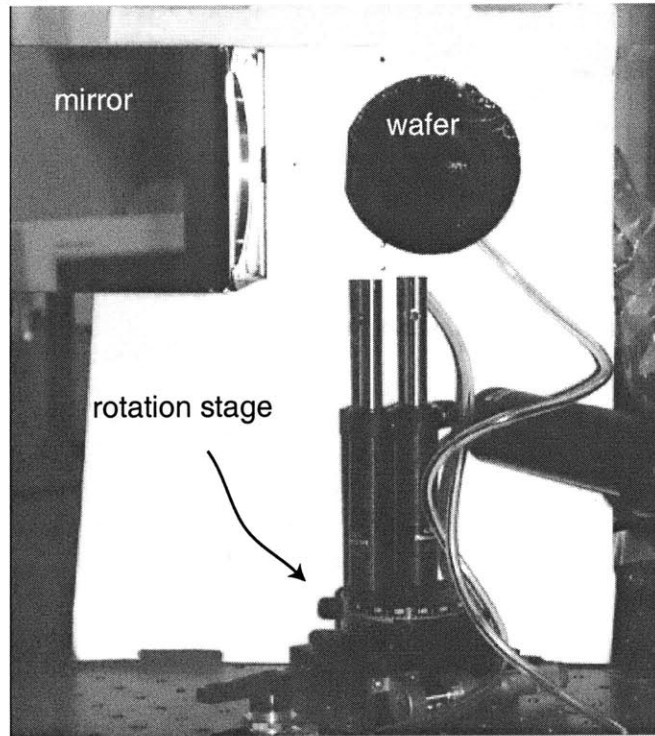
Figure 3.4: *The Lloyd's mirror interferometer.*

The wafer stage and mirror are shown in Figure 3.4. The interferometer was designed to accommodate up to a 4 inch diameter substrate. To maximize the linearity and contrast over a large area, the wafer is exposed one half at a time, with the other half covered. To expose the other side, the wafer is simply rotated 180 degrees. Although exposing the wafer in two parts allows an entire 4 inch diameter substrate to be exposed, the spatial phase of gratings is obviously uncorrellated for the two halves. Spatial phase coherence is limited to the area printed in a single exposure.

The Gaussian intensity profile in the plane of the exposure is shown in Figure 3.5. This is nominally twice the intensity of the beam, because of the reflected power from the mirror. At most, the exposed area will fall within a 5 cm radius of the optic axis. This corresponds to the exposure of a 10 cm wafer at normal incidence, the limit of long-period gratings. For shorter periods, the distance from the optic axis will decrease with the cosine of the incident angle. We can see that a relatively uniform exposure is achieved, with at most ~14% change in intensity over the exposed area. Thus, for a photoresist with a wide exposure latitude, the variation in linewidth over the entire 4 inch substrate is minimal.
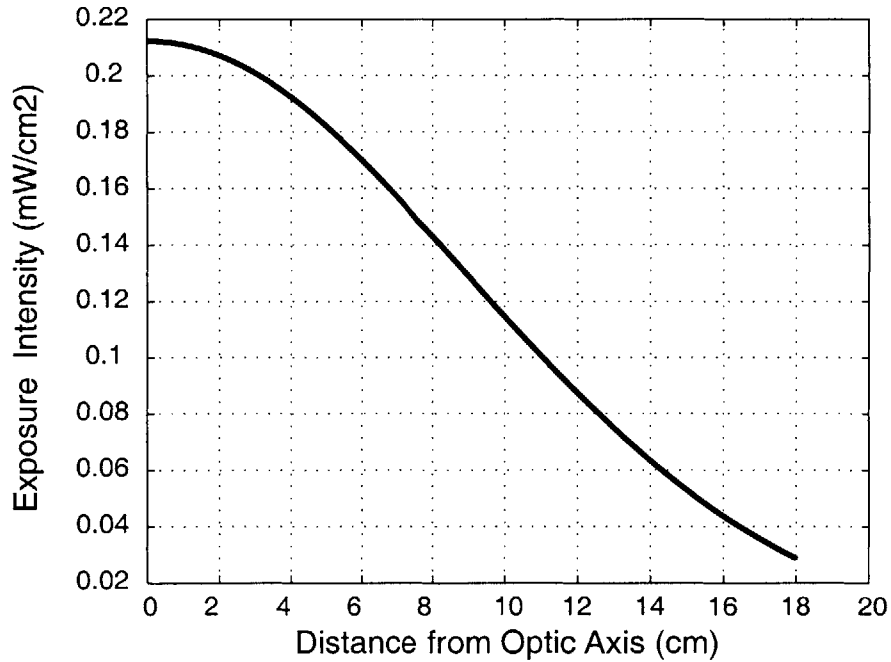
Figure 3.5: *The exposure intensity in the Lloyd's mirror configuration as a function of the distance from the optic axis.*

3.4) Coherence and Contrast

Contrast in the interference fringes in the Lloyd's mirror interferometer will never be perfect. Two factors contribute to this: reflection of less than 100% off the mirror results in an intensity difference in the two arms, and a path length difference inherent to the system which varies with the position on the substrate. To understand how these two factors influence the contrast, we can turn to the theory of partially coherent light, and the mutual coherence function (Eq. 3.1).

$$I = I_1 + I_2 + 2 \cdot I_1 \cdot I_2 \cdot |g_{12}| \cdot \cos(\phi)$$

(3.1)

I represents the sum intensity of two interfering beams at a given point in space, I_1 and I_2 are the intensities of the two interfering beams, and $|g_{12}|cos(\phi)$ represents the magnitude and phase of the coherence function, which encompasses the bandwidth of the source and any path length differences. For a set of interference fringes, the visibility *V*, or contrast, is defined as the difference between the maximum and minimum values of *I*, divided by the sum of maximum and minimum (Eq.3.2). These are found by

setting the cosine term to 1 and 0, respectively. As seen in Eq. 3.2, the visibility of fringes reduces to a product of an intensity term, and a term for path length and bandwidth.

$$V = \frac{I_{max} - I_{min}}{I_{max} + I_{min}} = \left(\frac{2 \cdot \sqrt{I_1 \cdot I_2}}{I_1 + I_2} \right) \cdot |g_{12}| \qquad (3.2)$$

When we examine the intensity term and the coherence term independently, we can get a better feel for how they each affect contrast. The coherence function will be examined in detail shortly; for now assume that its value is 1, and we look only at the effects of having different intensity in the two interfering beams. Figure 3.6 plots the fringe contrast as a function of the relative intensity ($R = I_1 / I_2$). The shape of the curve indicates that fringe contrast will remain high even for large differences in the intensity of the interfering beams. This forgiving shape is ideal for practical applications in interferometry, where it may be difficult to achieve equal intensity in both beams. In fact, the contrast remains above 0.9 even for relative intensities as low as 0.4. In the case of the Lloyd's mirror interferometer, the reflected beam will be a lower intensity than the directly incident beam because of the imperfect reflectivity of the mirror. We have chosen to use an aluminum mirror for its high UV reflectivity over a broad range of angles. The minimum reflectivity of the Al mirror is about 85%. For a relative intensity of 0.85, the contrast is 0.996, which allows us to effectively ignore the difference in beam intensity.
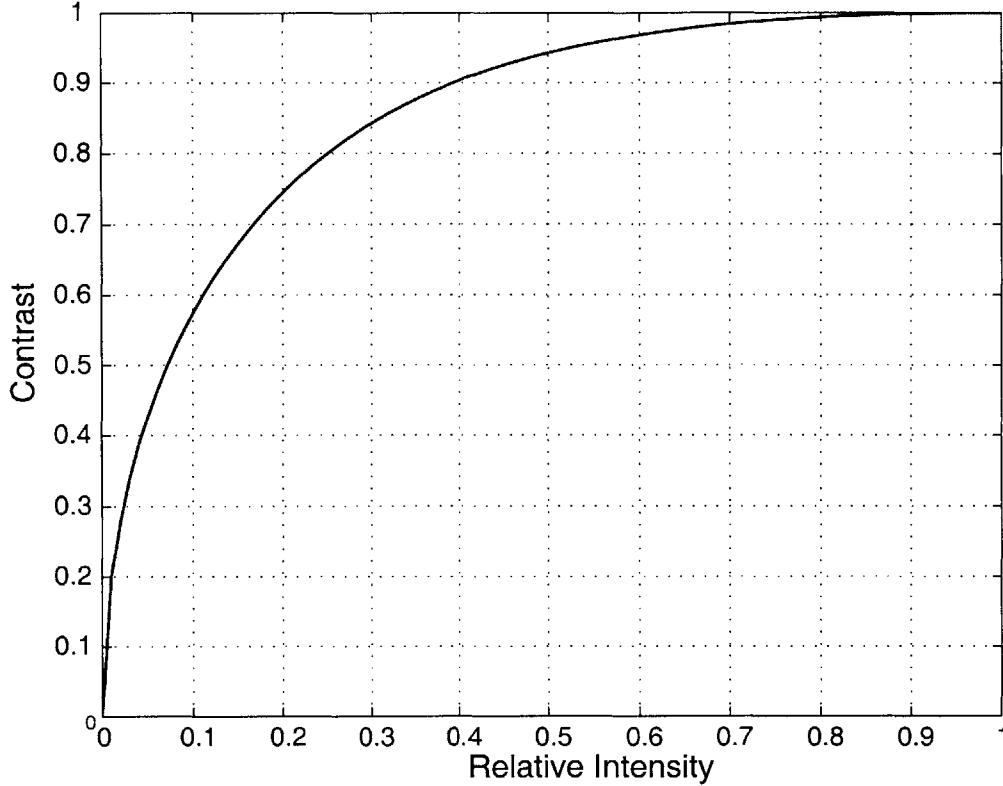
Figure 3.6: *The contrast of interference fringes as a function of the relative intensity of the two interfering beams*

If we now assume equal beam intensities, the contrast of the fringes reduces to the modulus of the mutual coherence function (Eq. 3.3)

$$V = |g_{12}(\tau)| \tag{3.3}$$

The mutual coherence function, defined in Equation 3.4, compares the similarity of a beam of light with a time-shifted version of the same beam. Mathematically, this is the autocorrelation function of the complex field $U(t)$, where τ is the time delay. The pointy brackets represent an inner product, or integral over all time.

$$g_{12}(\tau) = \left\langle U^*(t) \cdot U(t + \tau) \right\rangle \tag{3.4}$$

This integral can be quite difficult to solve. However, because we know the frequency spectrum of the source, we can take advantage of Fourier theory to provide an elegant solution. The frequency spectrum $F(v)$ is the Fourier

transform of the time domain signal $U(t)$. Knowing this, we can express the autocorrelation integral as the inverse Fourier transform of the squared frequency spectrum (Eq. 3.5).

$$g_{12}(\tau) = \Im^{-1}\left\{|F(v)|^2\right\}$$

(3.5)

Kimmon Electric LTd., the manufacturer of the HeCd laser used in the Lloyd's mirror system, specifies bandwidth of their laser at 1GHz. By modeling the frequency spectrum as a Gaussian profile with a FWHM bandwidth of 1 GHz centered around the 325 nm wavelength, we can solve for the coherence function with a simple inverse Fourier transform. The time delay τ converts to a length l through a scale factor of c, the speed of light. The fringe visibility for the Lloyd's mirror system (Eq. 3.6) is then simply the modulus of the coherence function (Eq. 3.3).

$$V(l) = e^{-\left(\frac{\pi}{c}\right)^2 \sigma^2 l^2}$$

(3.6)

Where c is the speed of light (3×10^8 m/s), l is the path length difference, and sigma is the standard deviation of the Gaussian bandwidth profile, 425 MHz. Figure 3.7 shows the profile of the decrease in fringe contrast as the path difference between the two arms increases.
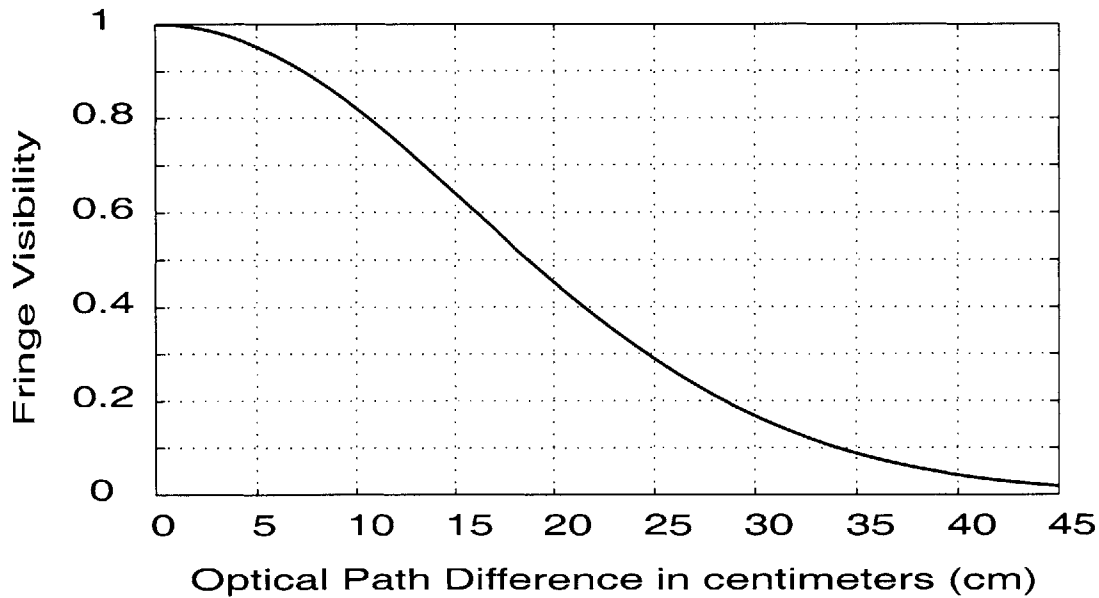
Figure 3.7: *Contrast of interference fringes as a function of optical path difference for a 1 GHz frequency bandwidth.*

The coherence length of the source can be found from an integral over all time of the squared visibility function scaled by the speed of light, seen in Equation 3.7. This calculation leads to a coherence length of 28.2 cm, which matches well with the manufacturers specification of 30 cm.

$$l_c = c \cdot \int_{-\infty}^{\infty} |g(\tau)|^2 \, d\tau \qquad (3.7)$$

The finite coherence length of the laser limits the maximum area of the exposure possible in this system. The geometry of the Lloyd's mirror configuration determines what the contrast will be on a given area of the substrate. The difference in optical path length between the two arms of the interferometer, the light directly incident on the substrate and that reflected off the mirror, is nonzero except at the corner between the mirror and the substrate. As the position on the substrate moves away from the center, the difference in path length increases. Therefore, the contrast of the interference fringes decreases in areas further away from the mirror. Also, the difference in path length increases as the spatial period of the grating decreases. Figure 3.8 depicts a cartoon of the two factors contributing to OPD in the Lloyd's mirror.
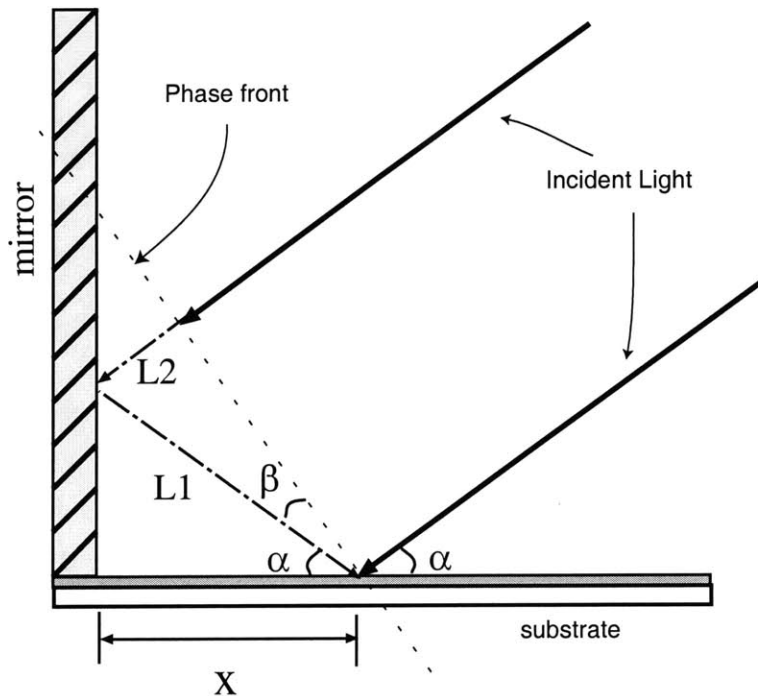
Figure 3.8: *Schematic of optical path length difference in the Lloyd's mirror*

The total OPD in the Lloyd's mirror can be thought of in two components, L_1 and L_2, which vary with x, the distance on the substrate away from the mirror and the angle of incidence of the incoming light. In this case, it is simpler to define the angle of incidence α from the substrate, rather than from the normal as is done for calculation of the spatial period. The L_1 component defined in Equation 3.8 represents the additional distance that the light must travel in the reflected arm after it hits the mirror.

$$L_1 = \frac{x}{\cos(\alpha)} \qquad (3.8)$$

The L_2 component, defined in Equation 3.9, represents the difference between when the light gets to the substrate and when it gets to the mirror. This can be positive or negative depending on the incident angle. L_2 is most simply represented in terms of the angle β ($\beta = 90 - 2\alpha$), which is seen in the cartoon to be the angle between the phase front and the reflected beam.

$$L_2 = L_1 \cdot \sin(\beta) \qquad (3.9)$$
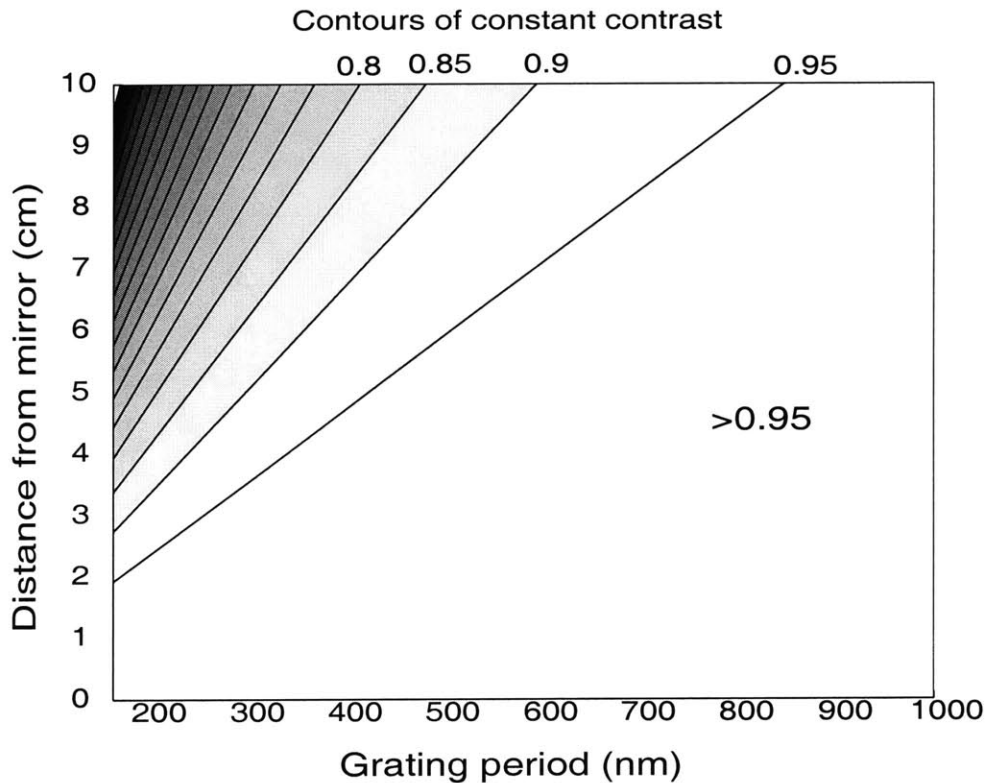
Figure 3.9: *Contours of constant contrast in the Lloyd's mirror interferometer*

The optical path difference (OPD) for a given distance x is simply the sum of L_1 and L_2.

$$OPD = \frac{x}{\cos(\alpha)} \cdot \left[1 + \sin(\beta) \right]$$

(3.10)

If we combine this measure of the OPD in the Lloyd's mirror with Equation 3.6, we can get a measure of the fringe contrast at a given point on the substrate for a given period. Figure 3.9 shows a contour plot of the contrast for distances up to 10 cm from the mirror, and periods between 163 nm (the theoretical minimum) and 1000 nm. Two interesting conclusions can be drawn from this graph. The contrast of the fringes will be high even far away from the mirror for large period gratings. This should be intuitively correct, because the light is incident almost normal to the substrate for large periods. The area of exposure for large period gratings will be limited by the size of the mirror rather than contrast of the fringes. For grating periods close to the lower limit, fringe contrast drops off rapidly as the distance away from the mirror is increased. As a practical example, consider a 200 nm period grating exposed on a 4 inch diameter wafer. The distance from the mirror of the outer edge of the wafer is 2 inch, or about 5 cm. From Fig. 3.9, the fringe contrast of a 200 nm period grating at 5 cm from the mirror is approximately 0.8., just barely sufficient to make a good exposure. However, if we move to a 165 nm period, close to the theoretical minimum period possible with a 325 nm laser, the fringe contrast drops to about 0.65 at 5 cm from the mirror. For low period gratings the fringe contrast will set the practical limit on exposure area. Under normal condition, though, the fringe contrast should not be a concern in exposures done on the Lloyd's mirror system. The maximum distance from the mirror of any substrate should be ~5 cm, and the practical lower limit on period is about 180 nm for other reasons.

3.5) References

[1]   E.H. Andersen, "Fabrication and Electromagnetic Applications of Periodic Nanostructures", Ph.D. Thesis, MIT, (1988)

[2]   J. Fererra, "Nanometer-scale placement in electron beam lithogaphy", Ph.D. Thesis, MIT (2000)

[3]   M. Farhoud, "Interferometric Lithography and Selected Applications", M.S. Thesis, MIT (1997)

[4]   H.I. Smith, Submicron- and Nanometer-Structures Technology. NanoStructures Press, Sudbury MA, (1994)

[5]   S. Tolansky, Introduction to Interferometry, Longmans, Green & Co., New York, 1955

[6]   H.H. Solak, D. He, W. Li, S. Singh-Glasson, F. Cerrina, B.H. Sohn, X.M. Yang, and N.P. Nealey, "Exposure of 38 nm grating patterns with extreme ultraviolet interferometric lithography". Appl. Phys. Lett. **75** 2328 (1999)

[7]   J. Ferrera, M.L. Schattenburg, H.I. Smith, "Ananlysis of distortion in interferometric lithography". J. Vac. Sci Technol. B **14** (6) 4009 (1996)

Chapter 4: Etching Magnetic Materials

4.1) Reactive Ion Etch

In Chapter 1, it was stated that it is extremely difficult to reactive-ion etch (RIE) magnetic materials. Although some effort has been devoted towards reactive processes for selected magnetic materials [1,2], the technology is not considered to be mature enough to be reliable. RIE processes are based upon a chemical reaction between the etch gas and the substrate which binds the substrate atoms into a volatile compound [3]. A good indication of whether or not a volatile by-product is possible can be found by checking the boiling point of compounds of the etch gas and substrate. Low boiling points indicate that the compounds will become volatile and an etch will occur, and high boiling points indicate either that an etch will only occur at high temperatures, or that it will not occur at all. Table 4.1 lists a couple of the simple compounds formed by common etch gasses with cobalt and nickel, and their respective boiling points [4]. Compounds formed by tungsten and silicon, easily etched materials, are included for comparison. As is clear from the table, the compounds formed by common etchants such as chlorine and fluorine are not volatile, and therefore do not enable RIE.

Material	Etchant	Compound	Boiling Point °C
Co	Fluorine	CoF_2	1400
Co	Chlorine	$CoCl_2$	1049
Ni	Chlorine	$NiCl_2$	Subl 973
W	Fluorine	WF_6	17.5
Si	Fluorine	SiF_4	-86

Table 4.1: *Boiling points of the compounds formed by selected materials and common reactive etch gasses.*

Another thing to consider when developing a process for etching magnetic materials is that there are a great variety of materials which may need to be etched. In addition to elements such as cobalt and nickel, alloys such as permalloy (NiFe), and CoCrPt are of great interest. In the development of MRAM devices, multilayer magnetic stacks consisting of very thin (<10 nm) layers can include a variety of magnetic and non-magnetic materials; examples are Co and NiFe, conductors such as Cu and Ta, and potentially even insulators such as SiO_2 or Al_2O_3. Even if one were available, an RIE process for etching Co is not guaranteed to etch other layers in the stack, nor is it guaranteed that the etch chemistry for one material will not damage other materials in the stack. From a practical standpoint, requiring a different etch process and mask design for such a wide variety of materials would require a large amount of tedious process development. Because of the lack of available RIE processes, as well as the potential lack of compatibility of RIE processes with a wide variety of materials, an alternate etch method must be used. Wet etching does not afford the necessary process control and deep sub-micron resolution. Broad ion beam etching, also known as ion milling, can provide the necessary resolution, as well as the ability to etch any material. However, there are some limitations to the technique which must be taken into account in order to use it successfully.

4.2) Ion Milling

Ion milling is a non-reactive etch process in which material is removed through physical sputtering. Sputtering refers to the removal of atoms from the target surface under bombardment by inert ions. If the energy of the incident ions is greater than a certain threshold energy, on the order of 10 eV, sufficient energy can be coupled to the atoms in the surface layers of the target that they will be ejected. The energy efficiency of the process is quite low, only high-energy atoms near the surface of the target will be ejected, those deeper in will have their energy lost as heat. One estimate indicates that about 98% of the incident ion energy is lost to heating and substrate damage [5]. The theory of sputtering has been well researched over approximately the past 50 years, although the primary application of sputtering has not been for etching, but for film deposition [6,7,8].

In the context of etching, there are a couple of problems that arise due to the non-reactive mechanism of the etch. First of all, there is a low etch

selectivity between the mask and target. Etch rates are determined in part by the sputtering yield of the material, that is, the number of ejected atoms from the material per incident ion. For all materials relevant to this work, the sputtering yield is on the order of unity, and thus etch rates are all within a factor of about 2 to one another. The etch rates for common ion milling conditions of materials that may be used in the course of this project are shown in Table 4.2.

For this reason, mask thickness must often be several times the thickness of the material to be etched. The ideal case is an infinite mask selectivity, a mask which is not affected at all during the etch. Reactive ion etching allows for much higher etch selectivities, often on the order of 10:1. A modification of ion milling, called reactive ion beam etching (RIBE), has been demonstrated in which the sputtering occurs in a background of reactive gas, often oxygen. In the case of oxygen, the reaction does not act to increase the etch rate of the target, but to decrease the etch rate of the mask. Oxides of the mask material can have much lower sputtering rates than the original metal. Also, oxygen is often preferentially sputtered out of the mask, but can be replaced from the atmosphere. Under these conditions, the selectivity of the etch can increase dramatically [9]. Properties of magnetic materials can be altered or destroyed by oxidation, which makes RIBE an unacceptable option for our experiments.

Material	Etch Rate Å/min
Co	550
Ni	660
Fe	530
Cu	1100
Pt	880
Cr	580
Ti	380
W	380
SiO2	400

Table 4.2: *Etch rates of commonly encountered materials for 500 eV normally incident argon ions with c current density of 0.40 mA cm^2 [10]*

Compounding the difficulty of low selectivity is a phenomenon referred to as faceting [11,12]. Faceting is when square corners of a feature become angled and etch at a greater rate than flat sections. Figure 4.1 shows a cartoon of a mask faceting, and the resultant change in the profile of the etched feature. Faceting occurs because the sputtering yield (and etch rate) are functions of the incident angle of the bombarding ions [13]. The top corners of squared sidewalls will develop a facet at an angle which corresponds to the maximum etch rate of the material, and this facet will propagate through the mask. The actual etch rate of a faceted mask can be much higher than the expected etch rate for normally incident ions. When the facet intersects with the target surface, linewidths can begin to narrow rapidly. Although faceting is a problem for all feature sizes, it is especially damaging in the smaller size regimes. When the facets from opposite sides of a feature intersect, the mask wears at a highly accelerated rate while the etch rate of the substrate is unchanged. Although it would be intuitive to increase the mask height to compensate for the increased wear due to faceting, this can be problematic for two reasons. This first reason is related to redeposition of substrate material on the mask, this will be addressed shortly. The second reason is the directionality of sputtered mask material. The mask material sputtered off the facets has a high probability of being ejected down towards the substrate, where it will redeposit and obscure sputtering of the substrate material. For taller masks, the facets are larger and more material gets deposited on the substrate. This can significantly decrease the etch rate of the substrate material, which only worsens the already low selectivity. One good example of the effect of faceting while etching magnetic structures is seen in the work of M.A.M. Haast, *et al* [14]. Also using a combination of inteference lithography and ion milling, their fabrication process for nominally cylindrical dots etched in CoNi/Pt multilayers resulted in extremely tapered pyramids.

The third main difficulty with ion milling, as eluded to earlier, is the redeposition of substrate material onto the sidewalls of the mask. The material ejected from the surface of the substrate under normally incident ions will have an angular distribution which follows a cosine law. There will be very little material ejected parallel to the substrate; the majority will be ejected away from the surface. Sputtered material will be ejected with a

preferential direction for bombarding ions with incident angles other than zero. This was seen in the case of the down-sputtered mask material described earlier in this section.
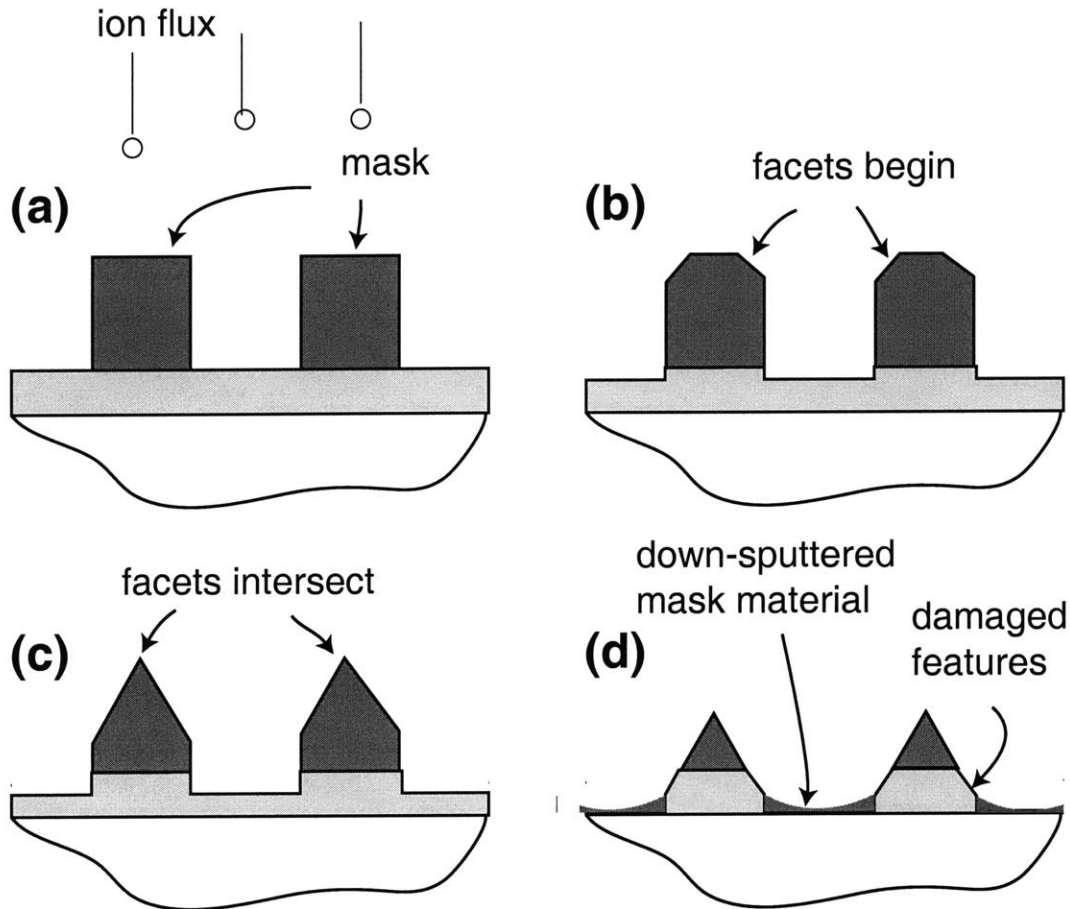
Figure 4.1: *Evolution faceting effects on the mask during ion milling.*

Any etch mask of non-zero thickness necessarily blocks the escape of some sputtered substrate material. The taller the mask, the more material will be blocked. The material clings to sidewalls of the mask and is not etched away due to the glancing angles of the incident ions. However, mask height in itself is not really the appropriate quantity to consider. The solid angle available for ejected material to escape determines how much of a problem redeposition will be, and this angle is determined by the ratio of mask height to mask spacing. To reduce redeposition, the mask height should be small in comparison to the mask spacing. The "wings" or "crowns"

which appear on a feature as a result of redeposition can cause a multitude of problems [15,16]. They cause a loss of linewidth control, inhibit further planar processing, and can radically alter the magnetic properties of the features. Figure 4.2 shows a cartoon of the redeposition process, and SEM micrographs of redeposition will be shown in Section 5.2.
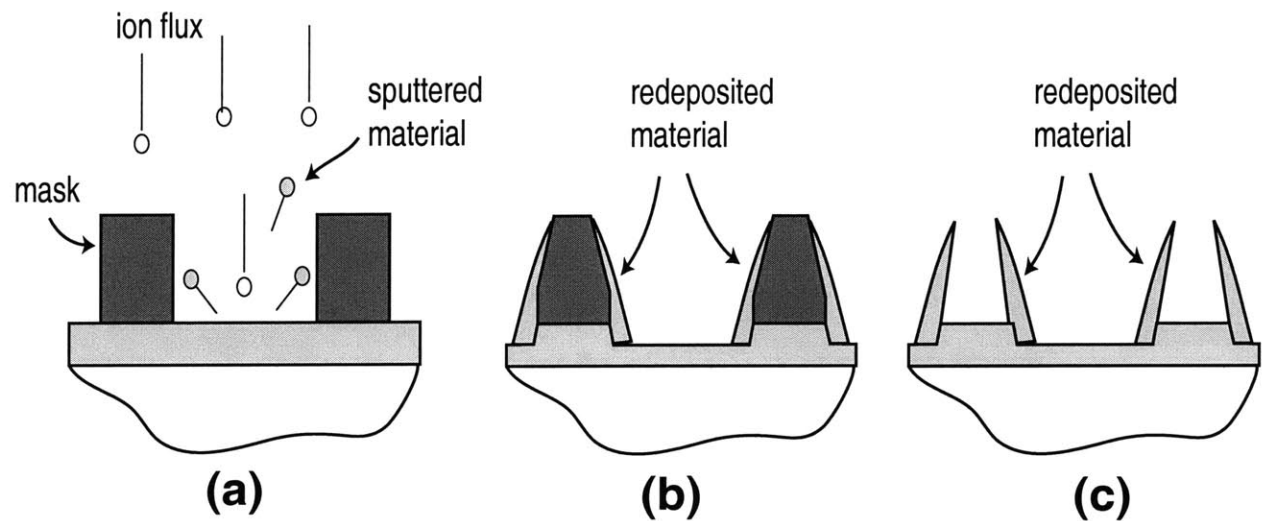
Figure 4.2: *Redeposition process. (a) Some sputtered material cannot escape and is deposited on the mask. (b) Redeposit after ecthing. (c) redeposit remains after mask is stripped.*

A conflict in mask design arises if the problems of faceting and redeposition are to be addressed simultaneously. To overcome the increased mask erosion from faceting, a tall mask is desirable, yet to overcome redeposition, a thin mask is desirable. Strategies which have been developed to overcome redeposition come with increased faceting and the resultant narrowing of features. One such technique finds an optimal angle for the incident ions at which the redeposited material is etched away at the same rate it is deposited [17]. An alternate implementation of the same idea begins with a mask that has tapered sidewalls rather than vertical sidewalls. In either case, faceting is enhanced and narrowing of the etched features is observed. Any successful ion milling situation must take into account these problems, although this often involves trading off one against the other.

4.3) References

[1]   K.B. Jung, H. Cho, K.P. Lee, J. Marburger, F. Sharifi, R.K. Singh, D. Kumar, K.H. Damen, S.J. Pearton, "Development of chemically assisted dry etching methods for magnetic device structures". J. Vac. Sci. Technol. B **17** (6) 3186 (1999)

[2]   M.S.P. Andriesse, T. Zijlstra, E. van der Drift, J.B.A. van Zon, "High speed anisotropic dry etching of CoNbZr for next generation magnetic recording" presented at the 44th International Conference for Electron, Ion, and Photon Beam Technology and Nanofabrication, (2000)

[3]   D.R. Lide ed., CRC Handbook of Chemistry and Physics, 73rd edition. CRC Press, London, 1992

[4]   J.W. Coburn, "Plasma Etching and Reactive-Ion Etching", American Vacuum Society Monograph Series, Ed. N. Rey Whetton, Amer. Inst. Phys., New York, (1982)

[5]   H.I. Smith, "Ion Beam Etching", Proceedings Symposium on Etching for Pattern Definition, The Electrochemical Society Inc., 133 (1976)

[6]   G.K. Wehner, G.S. Anderson, "The nature of physical sputtering", Handbook of Thin Film Technology, L.I. Maissel and R. Glang Eds. New York, McGraw-Hill, 1970 , Ch.3

[7]   G. Carter and J.S. Colligan, Ion Beam Bombardment of Solids, New York, American Elsevier, 1968.

[8]   P. Sigmund, "Theory of Sputtering I. Sputtering Yields of Amorphous and Polycrystalline Targets", Phys. Rev. **184** (2) 383 (1969)

[9]   M. Cantagrel and M. Marchal, "Argon Ion Etching in Reactive Gas," J. Mater. Sci., **8** 1711 (1973)

[10] H.R Kaufman and R.S. Robinson, Operation of Broad Beam Sources, Commonwealth Scientific Corporation, Alexandria VA, 1987

[11] J.P. Ducommun, M. Cantagrel, and M. Marchal, "Development of a general surface contour by ion erosion. Theory and computer simulation." J. Mater. Sci. **9**, 725, (1974)

[12]   O. Auciello, "Ion interaction with solids: Surface texturing, some bulk effects, and their possible applications". J. Vac. Sci. Technol. **19** 841 (1981)

[13]   G.K. Wehner, " Influence of the Angle of Incidence of Sputtering Yields", J. of Applied Physics **30** 1762 (1959)

[14]   M.A.M. Haast, J.R. Schuurhuis, L. Ableman, J.C. Lodder and Th. J. Popma, "Reversal mechanism of submicron patterned CoNi/Pt multilayers". IEEE Trans. Magn. **34** (4) 1006 (1998)

[15]   F.Rousseaux, D. Decanini, F. Carcenac, E. Cambril, M. Ravat, C. Chappert, N. Bardou, B. Bartenlian, P. Veillet, J. Vac. Sci. Technol. B **13** 2787 (1995)

[16]   N. Bardou, B. Bartenlian, C. Chappert, R. Megy, P. Veillet, J.P. Renard, F.Rousseaux, M. Ravat, J.P. Jamat, P. Meyer. J. Appl. Phys. **79** 5848 (1996)

[17]   P.G. Glöersen, "Ion-beam etching". J. Vac. Sci. Technol. **12** 28 (1975)

Chapter 5: Process Development

5.1) Introduction

So far, the components of a process for patterning magnetic nanostructures have been discussed individually: interference lithography and the Lloyds mirror interferometer, and the final etch via ion milling. The process for nanostructuring magnetic thin films can be considered most generally in three stages; lithography, pattern transfer via RIE to some type of mask, and ion milling to pattern the magnetic elements. Because each of these steps involves certain restrictions and peculiarities, finding a process which allows all three to be successful can be very subtle. Although the mechanisms of failure in IL and ion milling can be well understood, it is difficult to predict *a priori* whether or not a certain stack design will be successful. The following sections in this chapter examine stack designs which illustrate some of the points made earlier about IL and ion milling. These trials met with varying degrees of success, but each provided a clear indication of what was necessary in an improved design.

5.2) ARC Masks

The first attempt at a resist stack used the most familiar design. Known as the tri-layer resist process, it has been a staple of interference lithography at MIT for many years [1]. Similarly, polymer resist masks are probably the most common type used in ion milling. The resist stack and process steps are shown in Figure 5.1. The stack consists of a 200 nm thick layer of PFI-88 positive photoresist from Sumitomo, a 20 nm thick layer of evaporated SiO_x, over a 220 nm thick layer of ARC. In this case, the ARC used was ARC-XL from Brewer Science Inc., and its thickness was chosen to minimize back reflections into the resist. The entire stack was spun on over a 15-20 nm thick layer of cobalt on a silicon substrate. Based on the etch rate data in Table 4.1, it is assumed that pure cobalt will have sputter etch rates equal to or lower than any of the other magnetic or non-magnetic materials used in making GMR stacks, and thus provides an acceptable test

case for the stack design. The interference lithography is generally done at a period of 200 nm, printing features on the order of 100 nm.

Etch Step	Conditions	Time
1) RIE 20 nm SiO2 Interlayer	10 mT CHF3, 300 VDC, 150 W	1:30
2) RIE 300 nm ARC-XL	7 mT O2+He, 250 VDC, 150 W	8:00
3) Ion Mill 20 nm Co	500 eV Ar ions, 0.56 mA/cm²	5:00
4) Strip Remaining ARC	7 mT O2+He, 250 VDC, 150 W	8:00

Table 5.2: *RIE and ion milling etch parameters for the ARC mask process.*
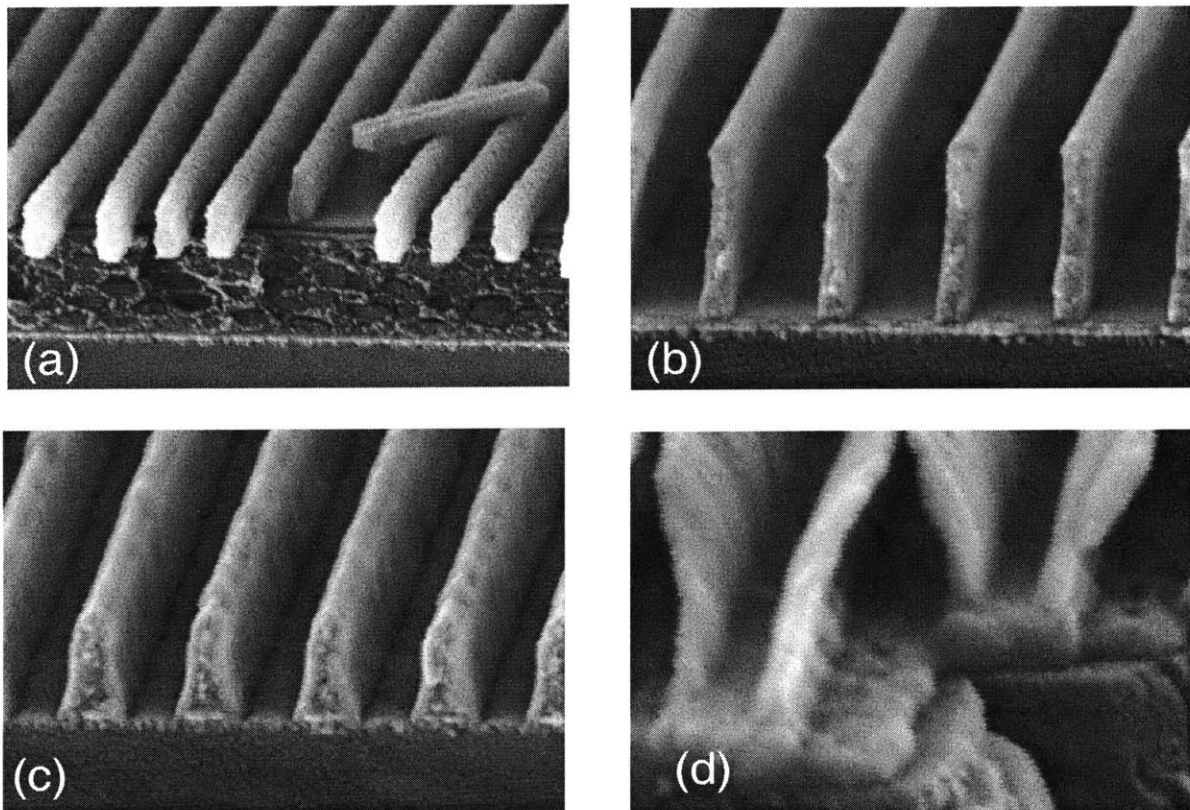

Figure 5.1: *SEM micrographs of a 200 nm period grating (A) resist profiles, (B) ARC mask, (C) mask after ion milling, (D) redeposit after ARC strip.*

The SiO2 interlayer is used to facilitate a high quality pattern transfer from the resist into the ARC. Resist and ARC, both carbonaceous polymers,

are essentially the same material in the context of RIE etch chemistry and will etch at about the same rate. However, there is a high selectivity between resist and oxide when etching in CHF_3 plasma, and a very high selectivity for oxide and ARC when etching in oxygen plasma. Thus, the pattern transfer is good from the resist to the oxide, and then from the oxide to the ARC. After the ARC etch, the resist is entirely removed, and the SiO_2/ARC combination can be used as the ion milling mask (Fig. 5.1b). However, as can be seen in Figure 5.1c,d, the ARC masks are not well suited for ion milling.

Even though the mask thickness is at 10 times the thickness of the cobalt layer, the two forms of redeposition described in in Chapter 4 combine to ruin this process. The angular dependence of resist etch rates has been reported as quite high, with a peak rate of about 2.5 times that of the normal incidence rate [2]. This leads to strong faceting of resist masks during ion-milling. Experience shows that this is also true for ARC masks, presumably because of their similar polymer chemistry. The down-sputtering of ARC material off the facets slows the etch rate of the cobalt in an unpredicatble manner. In Figure 5.1d, the etch of the cobalt layer is seen to be incomplete after an etch time of 4 minutes. This etch time is significantly longer than would be expected from the etch rate data in Table 4.1, and about twice as long as is seen in the etches described in Sections 5.2 and 5.3.

The down-sputtering of mask material combined with redeposition of the cobalt to increase the feature size by almost a factor of two in some cases. An example of this is shown in Figures 5.1b and 5.1c. The mask before ion milling has a width of about 60 nm, where after the ion milling it has widened to about 110 nm, almost double its original size. The redeposition is also clearly apparent in Figure 5.1d after the ARC has been stripped. The large wing-like structures protruding upwards from the grating lines are a mixture of ARC and cobalt, and are not easily removed.

Although the simple tri-layer stack is well-tuned for the IL and pattern transfer steps, the ARC proves to be a dismal mask for ion milling. The failure can be attributed to the high aspect ratio of the mask which created a situation of heavy redeposit of both mask and target material. The high angular dependence of the ARC etch rates only served to worsen the problem through severe faceting.

5.3) Titanium Hardmask

The mode of failure of the ARC mask indicated that the next attempt should use a thin mask of a material which has a low variation of sputtering rate with incident angle. The material selected was titanium, for a couple of reasons. Titanium has a comparatively low base sputtering rate at normal incidence, giving it a nominal etch selectivity of 1.44 with cobalt [3]. Also, Ti has been reported to have a low variation in sputtering rate with incident angle [4]. There are a number of materials which have both a low base sputtering rate and a low variation with incident angle, carbon films and alumina (Al_2O_3) are examples. However, we must remember that the mask material must be easily patterned and stripped away after ion milling. The list of process compatible films with advantageous sputtering properties then becomes quite short. Titanium has the potential to be etched with RIE; titanium tetrafluoride (TiF_4) will sublime at 278 C [5]. Although this etch requires some heating of the substrate, it is certainly not outside practical bounds.

Etch Step	Conditions	Time
1) RIE 20 nm SiO2 Interlayer	10 mT CHF3, 300 VDC, 150 W	1:30
2) RIE 220 nm BARLi ARC	7 mT O2+He, 250 VDC, 150 W	4:30
3) RIE 25 nm Ti hardmask	10 mT CF4, 300 VDC, 150 W	6:00
4) Strip remainig ARC	7 mT mT O2+He, 250 VDC, 150 W	3:00
5) Ion Mill ~20 nm Co or multilayer stack	500 eV Ar ions, 0.50 mA/cm^2	2:00
6) Optional: Strip remaining Ti mask	10 mT CF4, 300 VDC, 150 W	4:00

Table 5.2: *RIE and ion milling etch parameters for ion milling thin magnetic films with titanium hardmasks.*

For this process, a 25 nm thick film of Ti was deposited directly on the 20 nm thick Co layer. The tri-layer resist stack described in section 5.1, was spun on top of the Ti. A different ARC, AZ BARLi, was used for these experiments which would allow a slightly thinner (220 nm) film to be used.

The BARLi ARC also has higher RIE rates than the Brewer Science ARC's used previously, allowing shorter etch times. Rather than being used directly as the ion-milling mask, the ARC in this process was used as an RIE mask for the titanium, and then stripped away. Only the 25 nm Ti was used as the ion milling mask. Table 5.2 lists all of the etch steps and conditions, a few of which are shown in Figure 5.2.
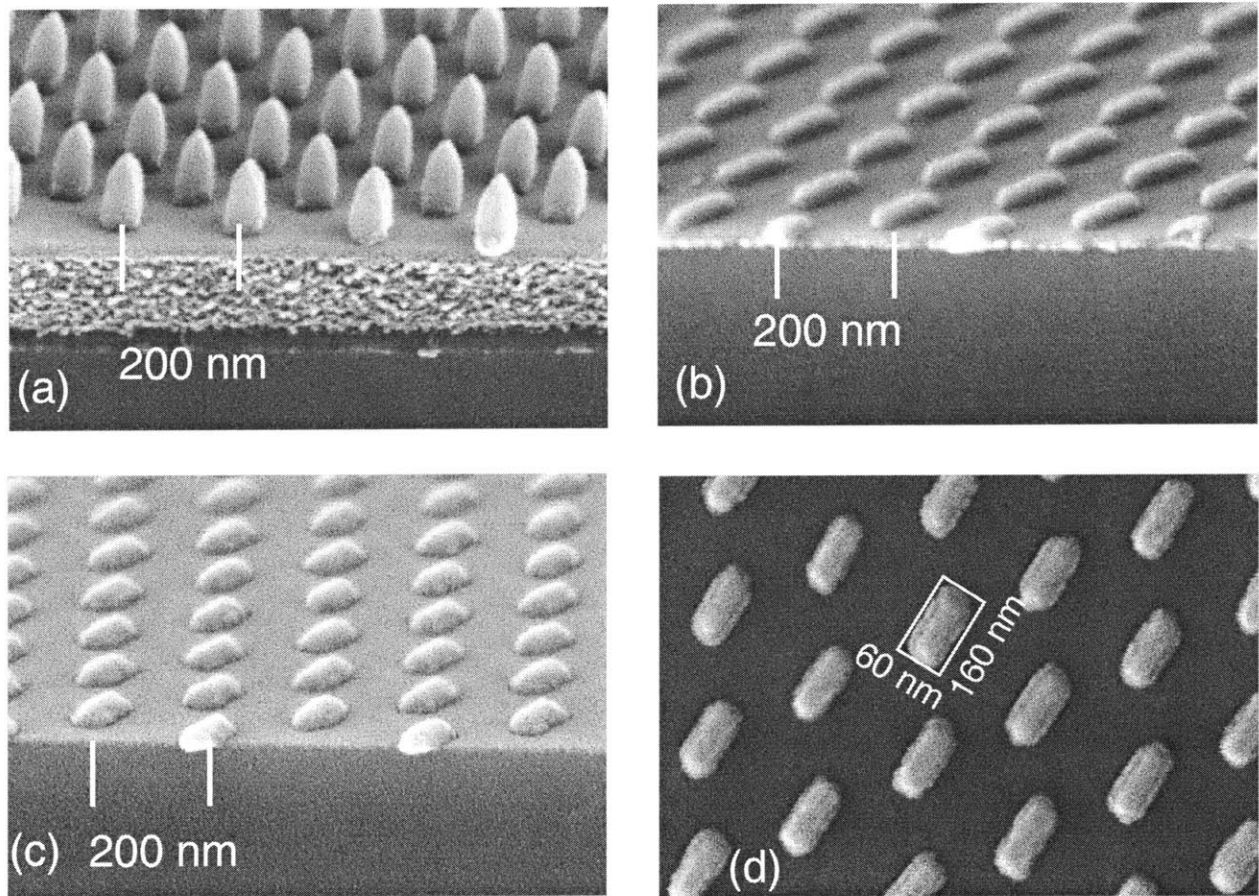
Figure 5.2: *SEM micrographs of ellipses patterned with Ti hardmask process: (a) resist profiles, (b) Ti mask before ion milling, (c) nanomagnets with mask after ion milling, (d) top view of 5.2c.*

The micrographs in Figure 5.2 depict a couple of important steps in the process. Rather than showing gratings in cobalt, which illustrated the shortcomings of the ARC mask more clearly than dots would, the micrographs for this process depict ellipsoidal structures etched into a multi-layer stack. The thin film stack consists of (starting at the bottom): 5 nm

Cr/ 5 nm Cu/ 5 nm Co/ 3 nm Cu/ 2 nm Co. The chromium underlayer is primarily for adhesion and the 5 nm copper serves to orient the crystal growth in the 5 nm cobalt film. The Co/Cu/Co stack at the top is the spin valve as described in Chapter 1. Based on the etch rates in Table 4.1, chromium and cobalt will sputter etch at essentially the same rate, while the copper etches roughly twice as fast. The total etch time for this multilayer should be only slightly less than that of a single 20 nm film of cobalt.

The micrographs in Figure 5.2 show that the hardmask process allows for the effective transfer of a resist pattern through to an etched magnetic film. Figure 5.2a shows the initial resist pattern, an array of ellipses exposed using IL. The method of exposure in this case was the off-orthogonal grid; 200 nm gratings exposed at 45 degrees to one another. The resist profiles look round because they are viewed along the long axis at a steep viewing angle, about 60° above the plane. Figure 5.2b shows the Ti mask after the ARC has been stripped away, but before ion milling. The mask shape and dimensions are slightly smaller than the initial resist patterns due to erosion of the ARC during the long Ti etch. Figure 5.2c shows the structures etched into the multilayer after ion milling, with the Ti mask left in place. The choice was made in this case to leave the mask intact after the etch to provide a protective layer over the thin 2 nm Co layer on top of the spin valve to prevent oxidation. The mask shows some rounding due to faceting, but not enough to adversely affect the etch. The dimensions of the structures are essentially unchanged by the ion milling process. Figure 5.2d shows a top view of the structures in 5.2c; the aspect ratio is approximately 2.7. In comparison to the ARC mask, the use of a titanium hardmask has been a great success. Linewidth control has been achieved for sub-100 nm features, etch times are reduced by lack of downsputering, and redeposition has been eliminated.

Unfortunately, despite the apparent success of this process, it has certain drawbacks which make it undesirable for further use in the development of MRAM devices. The hysterisis loop of the structures from Figure 5.2 is seen in Figure 5.3. The shape anisotropy caused by the elliptical nature of the particles is seen in the difference between the long axis and short axis hysteresis loops. However, there is no evidence in either loop of the two-layer switching behavior which would lead to magneto-resistance. This means that although the multi-layer films have been

physically patterned successfully, the etching process fails to preserve their magnetic properties. There is evidence that high temperatures can cause a deterioration of the multilayer properties of magnetic thin film stacks. The mechanism for this damage is assumed to be diffusion, which causes the cobalt layers to become coupled, although this is not known for sure. Two steps in particular in this process can be flagged as potentially damaging.
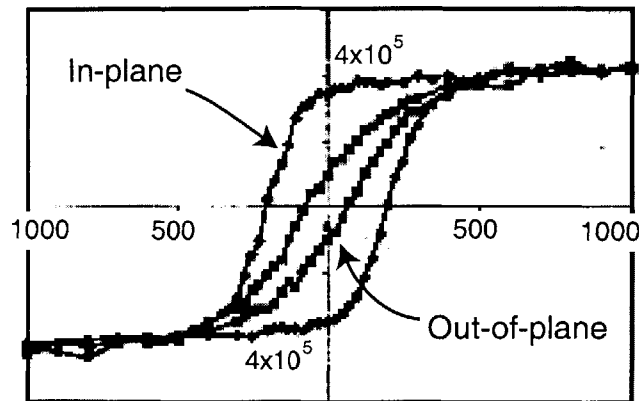

Figure 5.3: *The hysteresis loop of the multilayer ellipses shown in Figure 5.2 c,d.[6]*

First, the anti reflection coatings are designed to be baked at temperatures of about 175°C, although only for about 1 minute. Although this may not seem like too high a temperature or too long of a time, a comparison of the hysteresis loops of spin valve structures before and after an ARC bake shows that significant damage can be done. Figure 5.4 shows two hysteresis loops for unpatterned bulk film stacks, in Fig. 5.4a is the loop for an unpatterned spin valve film with no processing done. The two layer switching is clearly seen as a notch in the curve. If an ARC layer is spun on and baked at 180°C for 60 seconds, and no further processing is done, the two layer switching is destroyed, as shown in Figure 5.4b. The two cobalt layers have become coupled, and no longer switch independently of one another.
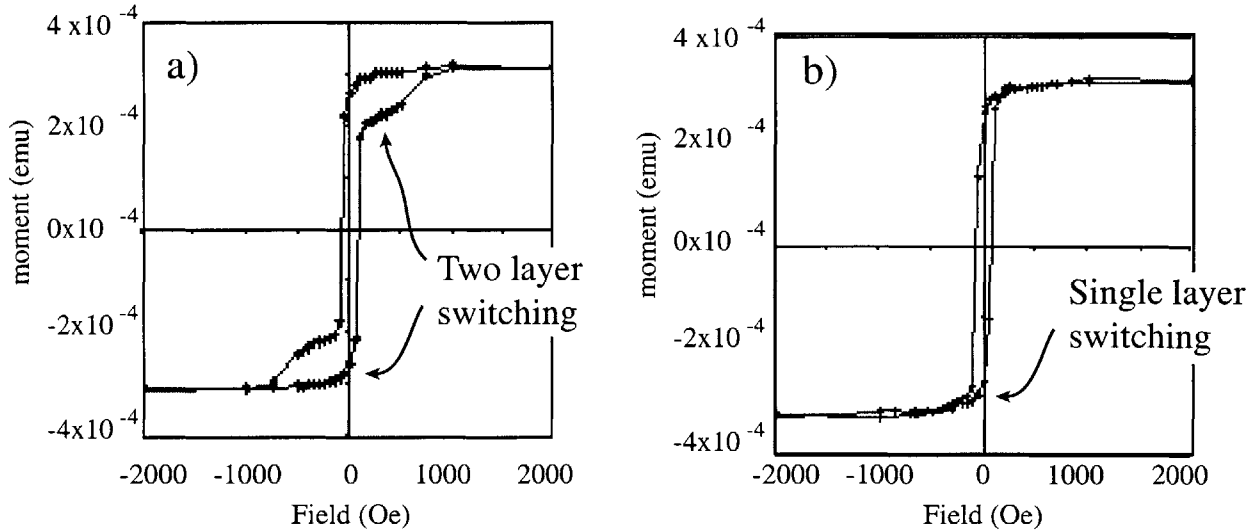
Figure 5.4: *Hysteresis loops for bulk spin valve films before and after an ARC bake.[7]*

The ARC bake is not the only step which causes concern, though. Every RIE step generates heat which can be potentially damaging. Some steps can make use of helium backside cooling of the substrate during the etch. In the case of the ARC etch, backside cooling can help improve the etch profiles by reducing undercutting. However, the titanium etch cannot be adequately cooled because of the high temperatures necessary for sublimation. Although the Ti etch was optimized for the available tools, the etch rate was quite slow. Approximately a 6 minute etch was necessary to clear through the 25 nm Ti layer an etch rate of 4 nm/min. The long etch times combined with the lack of cooling, serve to heat the substrate substantially more than other RIE steps in this process. Moreover, this step is necessary twice, once to pattern the Ti mask and once to strip it away after ion milling. Although the data is not presented here, further tests on the samples shown in Figure 5.2 indicate that the post-ion-milling strip of the Ti mask furhter degrades the hysterisis loop of the dots. The exact temperature of the substrate is unknown during this etch, but the high heat sensitivity of the films makes eliminating any high-heat steps a priority.

For other magnetic films which are less sensitive to damage by heat, this process is more successful. Films of a single material for instance, should be unaffected by the temperatures in this process. Other multilayer films made by IBM with a strong out-of-plane anisotropy were patterned into

circular dots using this process. The multilayer in this case was a 10x repetition of 0.3 nm Co/ 1 nm Pt, with a 20 nm Pt underlayer and a 2 nm Pt cap. The total thickness of the stack is 35 nm, but the etch rate of Pt is about 175% that of Co, so like the spin valves, the stack is equivalent to about a 20 nm thick layer of Co. SEM images of the Ti mask before ion milling and the finished dots are shown in Figure 5.5 a,b. Figure 5.5c shows the out-of-plane hysteresis loop of the dots and the loop for the bulk film before patterning. In both cases, the existence of the out-of plane loop indicates that the multilayer structures are functioning as designed.
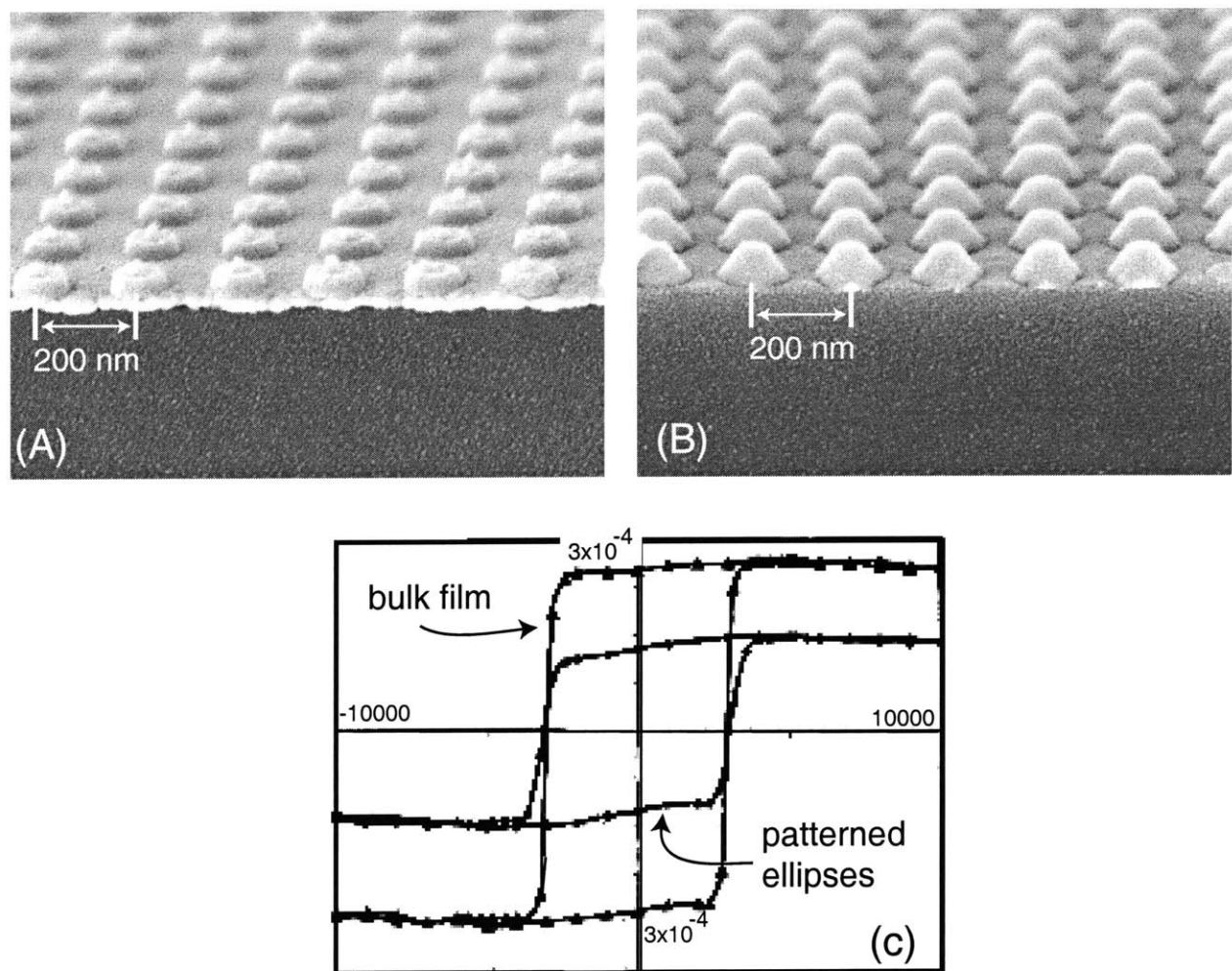

Figure 5.5: *Circular dots in IBM multilayer stack: A) titanium mask before ion milling, B) Dots after milling with Ti mask intact, C) Out-of-plane hysterisis loop of the bulk film and the patterned dots [8].*

Just the shape anisotropy of the dots would give an in-plane easy axis. However, the bulk film and dots have a perpendicular easy axis due to the multilayer structure. To a certain extent, the multilayers have survived the patterning process, although two aspects of the hysteresis loops indicate that they have been damaged in some way. The saturation moment (M_s) of the patterned dots is less than that of the bulk film, which is to be expected due to the lower total volume of the dots compared to the bulk film. However, M_s has decreased more than can be attributed to a volume change alone. The most probable cause is heat induced interdiffusion between the layers which has degraded their magnetic properties. Also, the loop of the dots is much less square than the loop of the bulk film, indicating a distribution of switching fields for the dots, indicating that the damage to the multilayers was uneven. Ideally, all of the dots would be identical, and switch at the same field. Another possibility is that the sloped sidewalls of the dots (Fig 5.4b) contributes to interaction between the layers which is not ideal. The sloped sidewalls indicate that faceting has occurred on the mask, and dimensional control may be an issue for certain kinds of structures.

The titanium hardmask process has proven to be partially successful As hoped, the use of a thin mask resistant to faceting and with low base sputtering rates has allowed the succesful ion milling of magnetic films. The problems of faceting and redeposition have been largely conquered with this approach. However, the choice of titanium as the hardmask material has increased the complexity of pattern transfer into the mask, and potentially leads to heat damage in multi-layer stacks. Also, the use of a high temperature ARC bake has been shown to be damaging to the magnetic properties of multilayer stacks. Through the addition of a hardmask to the tri-layer resist stack, this process has solved the lithographic and ion milling problems with an excessive "brute force" approach. The next phase of development was directed towards reducing potential for heat damage through a minimized design.

5.4) Thin Resist Processes

The goal of the next phase of design was to produce a stack which required the absolute minimium number of process steps, and only included

steps which could be done without elevated temperatures. Considering which of the layers in the Ti process stack were absolutely necessary, and which elements only facilitated another step, we can begin with the simplest possible case. Two layers which must be included in any stack, for obvious reasons, are the magnetic film and the photoresist. Anything in addition to these two layers only serves as an aid in either the generation of the pattern in the resist or the transfer of the pattern to the magnetic layer. In this light, the Ti hardmask process seems bloated with additional complexity. In Section 5.1 it was shown that a polymer mask such as resist is not appropriate for etching deep sub-micron features by ion milling. Therefore, a hardmask between the resist and the magnetic films must join the list of necessary layers. The ARC was shown to be problematic in the previous section, so it would be preferable to work without it. Without the ARC layer, the SiO2 interlayer is unnecessary.

Considering the utility of the ARC in suppressing standing waves in the resist, a successful exposure without an ARC will require some modification of the way the IL is done. The vertical standing wave adversely affects resist profiles by scalloping the sidewalls. Careful thought reveals that this will only be a problem if the high intensity nodes of the vertical wave occur within the resist layer. If the resist is made thin enough that the high intensity nodes occur in the air above the resist, then presumably the effect of the vertical wave on the resist will be diminished.

On a highly reflective surface, such as a metallic hardmask, the vertical wave forms with a null near the resist/metal boundary, and peaks 1/2 wavelength away. If the resist thickness is designed to be ~1/4 wavelength thick, then the peak of the vertical wave will occur outside of the resist volume. Using Equation 2.2, the period of the vertical standing wave can be calculated as 154 nm for a 200 nm period grating in PFI-88 resist (n=1.79) exposed in the 325 nm light of the Lloyds mirror interferometer. To avoid over thinning, a 50 nm thick layer of resist was used, which is slighly more than 1/4 of the period of the vertical wave.

Round Resist Profile

200 nm

25 nm W/20nm Co

Etched W Profile

200 nm

20nm Co
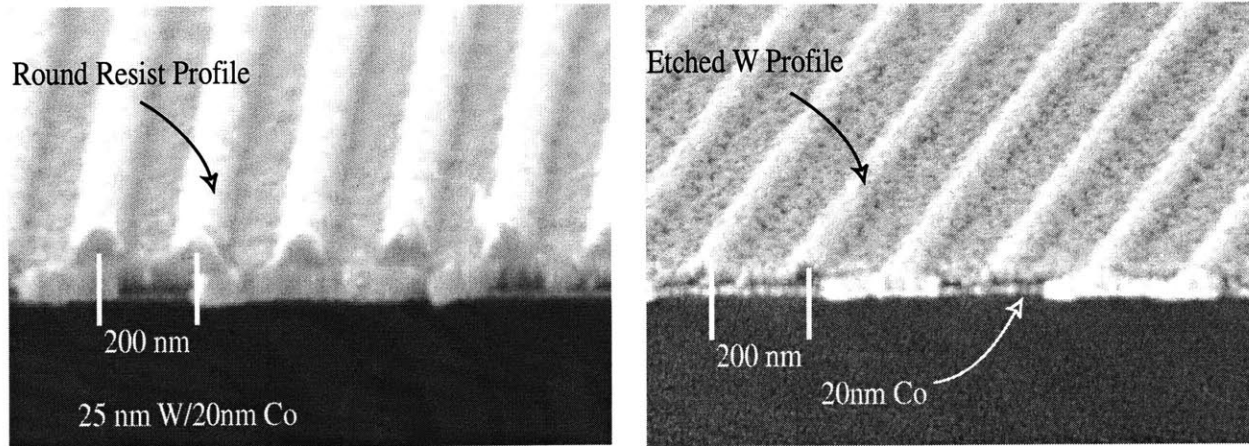
Figure 5.6: *200 nm period grating: (a) lines exposed in thin resist directly over tungsten. (b) Lines in tungsten after an attempted pattern transfer. The resist is destroyed before completion of the W etch.*

The hardmask material chosen to replace titanium was tungsten. Tungsten has the same properties of low base etch rate at normal incidence (See Table 4.1), and low variation of etch rate with incident angle [9]. In contrast to titanium, tungsten forms a truly volatile gas, tungsten hexafluoride (WF$_6$ has a boiling point of 17.5 °C), which should enable a much easier RIE than Ti [5]. Figure 5.6 shows an SEM micrograph of a grating exposed using the thin resist process and the transfer to the tungsten layer underneath. The resist profiles in this scheme are severely rounded (Fig 5.6a). This can be attributed to the rapid increase in intensity in the vertical direction. The rounded profiles on their own do not immediately make this a bad process. If the pattern could be easily transferred to the tungsten layer underneath, then the initial resist profile would not be cause for concern. In this case, though, a successful pattern transfer to the tungsten layer underneath proved impossible. The gratings seen in Figure 5.6b are the result of an optimized RIE process, yet the 25 nm thick W layer is not cleared and the resist has been completely etched away. The gas mixture used to etch the tungsten, about 85% CF$_4$ and 15% O$_2$, also attacks the resist. The rounded profile of the resist mask transfers to a rounded W profile, but the selectivity is too low for the tungsten to clear before the resist is destroyed.

As is done when etching SiO_2 with resist masks, higher selectivity can be gained for some fluorine based chemistries by adding hydrogen, for instance using CHF_3 as the etch gas instead of CF_4. In the case of a tungsten etch though, CHF_3 is simply not an appropriate choice. Etch rates were observed to be close to zero when testing CHF_3 as an etch gas for W. To explain this, we can consider chemical vapor deposition (CVD), which is in some ways a complementary process to RIE. Tungsten films can be deposited using CVD starting with gaseous WF_6, the same gas formed during the RIE of W. The gas is flown over the substrate and reduced using hydrogen, and the W slowly forms a film over the substrate. Hydrogen content in the RIE, then, can be seen as acting to inhibit the tungsten etch by reclaiming the W out of its volatile form.

Neither the lithography nor the pattern transfer in this process was successful enough to even determine how well tungsten functions as an ion milling mask; it was just too simple. The resist profiles are too thin and too rounded to enable an effective transfer of the pattern to the tungsten mask. If we consider adding another layer to the stack, it should be chosen to either improve the resist profiles or enhance the pattern transfer.

By resurrecting an old idea, which predates the use of absorbing ARC's, we can use a single thin-film to improve both the resist profiles and the pattern transfer into the tungsten. Efremow *et al* [10,11] proposed in 1981 the use of a thin layer of SiO_2 underneath a thin resist to improve resist profiles. Unlike the absorbing and interference ARC's that were described in Chapter 2, the intent of this technique is not to reduce the reflected power in the resist, but rather to shift the phase of the vertical standing wave. The rounding of the resist profiles seen in Figure 5.6 was attributed to the increasing intensity towards the top of the resist. By shifting the peak of the vertical wave so that it lies near the bottom of the resist, the developed resist profiles become much more square. Figure 5.7 depicts a comparison of the phase of the vertical standing wave with and without phase shifting, and the developed profiles with and without a phase shifting oxide layer.
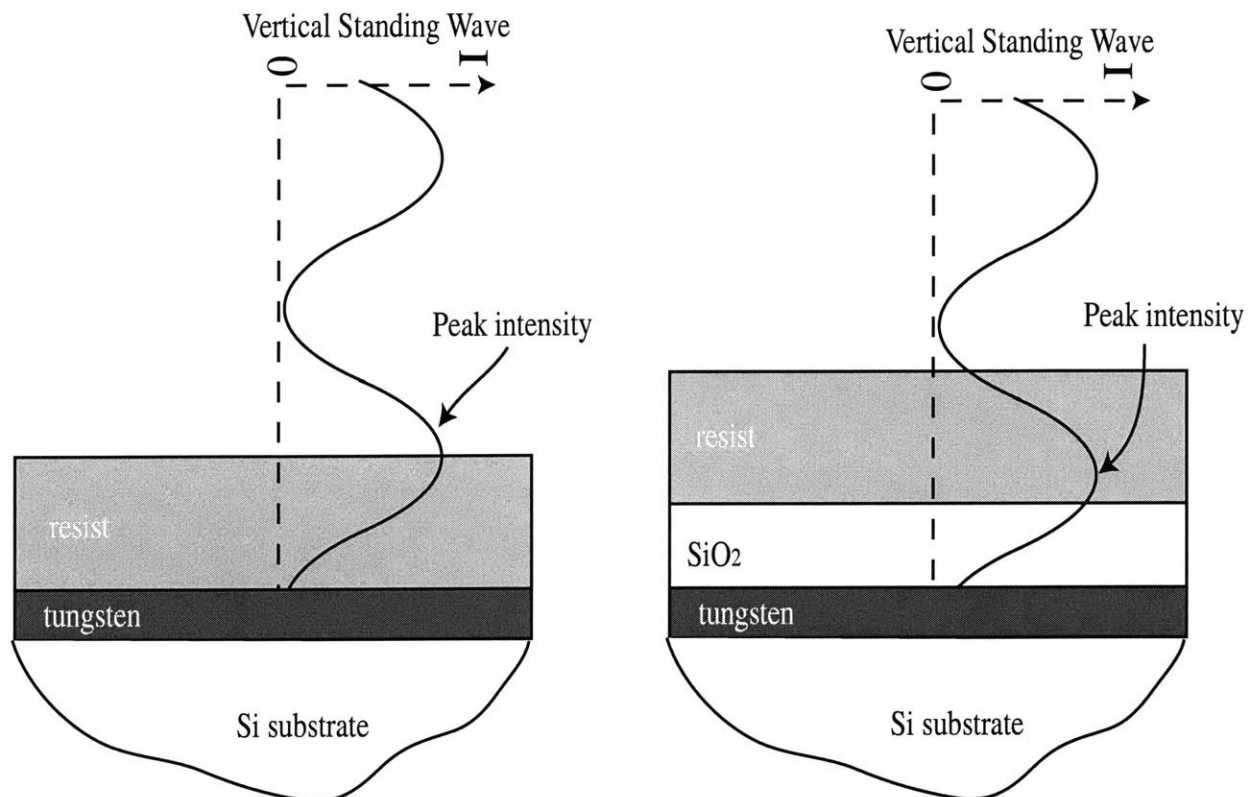
A) Intensity profiles during exposure, with and without phase shifting oxide layer
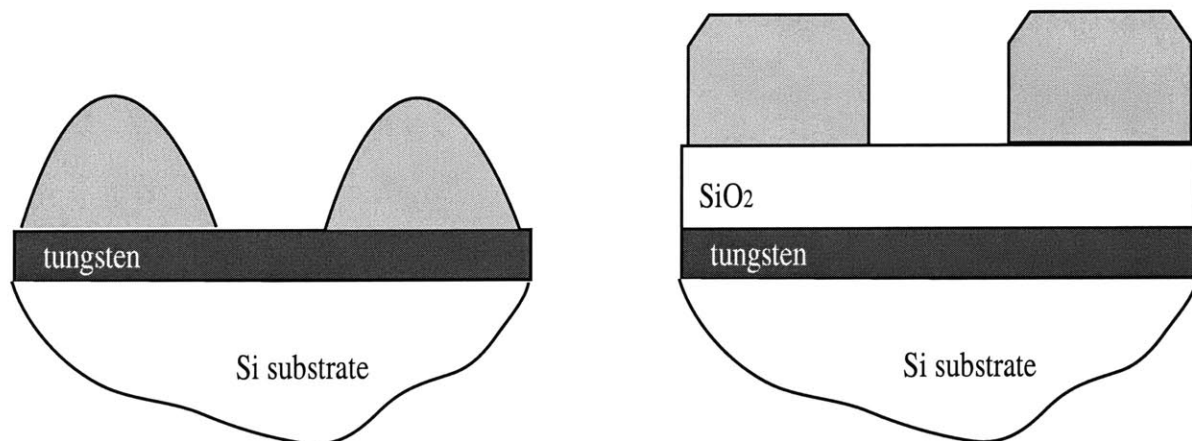
B) Resist profiles after development, with and without phase shifting oxide.

Figure 5.7: *A comparison of the exposure and development of thin resist stacks with and without a phase shifting oxide layer.*

With no phase shifting layer, the intensity in the resist is highest at the top and lowest at the bottom. This gives rise to the rounded profiles as seen in Figure 5.6. However, with the addition of the phase shifting layers the intensity decreases towards the top of the resist and much more square profiles are obtained. Figure 5.8 shows calculations of the vertical intensity in the resist starting at the lower resist boundary and moving upwards. The same simulation program described in Chapter 2 was used to calculate the vertical intensity profiles, details of these calculations are found in Appendix B. It is clear from the calculations that the intensity in the resist behaves as predicted. In the case where no phase shifting layer is used (Fig 5.8a), the intensity is minimum near the bottom of the resist, and increases towards the top. When a 30 nm SiO2 phase shifting layer is added, the intensity profile moves to the more desirable case of decreasing towards the top of the resist.
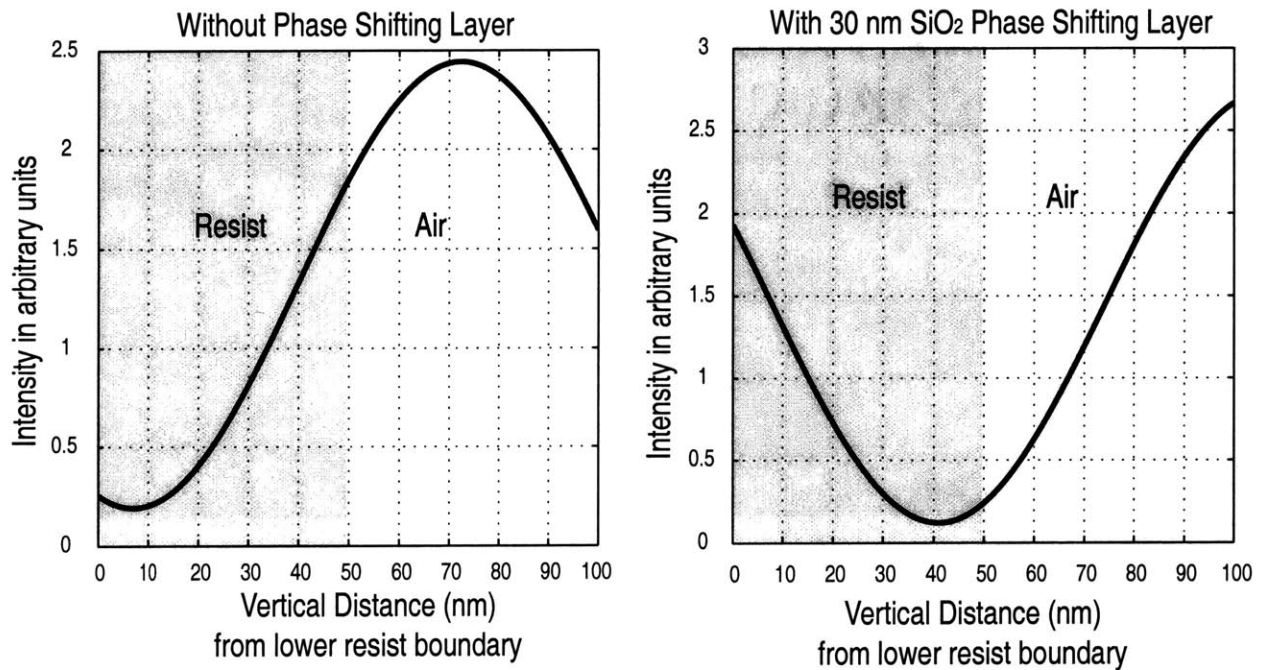

Figure 5.8: *A comparison of the vertical intensity profile in the resist: (A) resist is spun directly on top of W hardmask, (B) a 30 nm SiO₂ phase shifting layer is used.*

In Chapter 2, dose calculations for the photoresist were presented which included a term to account for the back reflections into the resist. At the time, this appeared to be an extraneous term because a properly

designed ARC eliminates these back reflections. The thin phase shifting resist stack, however, has back reflections on the order of 50%. For this process, the back reflections must be taken into account to ensure a good exposure.

Another advantage of the oxide layer is that it facilitates a good etch of the tungsten mask under the right conditions. As mentioned earlier, the resist to oxide etch using a CHF_3 plasma allows an excellent pattern transfer due to the high selectivity of this chemistry. The combined resist/SiO_2 mask is sufficient to pattern the thin W layer with good linewidth control and square sidewalls. However, the plasma parameters are important to making this etch successful. The 88% CF_4 and 12 % O_2 mix maximizes the free fluorine in the plasma. The etch rates of tungsten increase with oxygen content up 12%, while the etch rates of SiO_2 do not change as much. Also, etch rates of SiO_2 are much more dependent on the energy of the bombarding ions, determined by the bias voltage of the plasma, than the etch rates of tungsten. Therefore, a low bias plasma is used to reduce the etch rates of the oxide without decreasing the etch rate of the tungsten. Table 5.3 shows the etch parameters used during this process.

As with the titanium masks, the resist and oxide are stripped off of the tungsten before ion milling to give the thinnest mask possible. A series of SEM micrographs shows the complete process, from resist exposure to ion milling in Figure 5.9.

Etch Step	Conditions	Time
1) RIE 30 nm SiO_2	10 mT CHF_3, 300 VDC, 150 W	1:30
2) RIE 25 nm W hardmask	20 mT CF_4 (85%) and O_2(15%), 60 VDC, 50 W	2:15
3) Strip remaining SiO_2	10 mT CHF_3, 300 VDC, 150 W	1:00
4) Ion Mill ~20 nm Co or multilayer stack	500 eV Ar ions, 0.40 mA/cm2	2:30
5) Optional: Strip remaining W mask	20 mT CF_4 (85%) and O2(15%), 60 VDC, 50 W	1:30

Table 5.3: *RIE and ion milling etch parameters used in the thin phase-shifting resist process.*

The series of micrographs in Figure 5.9 depicts a 200 nm grating at each of the various steps in the process, beginning with the resist profiles in Fig 5.9a. After the pattern is transferred through the SiO_2 and into the tungsten, the grating lines are shown in Fig. 5.9b before stripping the SiO_2. After the oxide is removed, the tungsten mask before ion milling is seen in Fig 5.9c, and a top view is shown in Fig. 5.9f. The linewidth of the tungsten mask is 75 nm. After ion milling in 500 eV argon ions for 2 min. 30 sec., the lines are seen in Fig. 5.9d. A top view of the lines at this point is shown in Fig. 5.9g, and the linewidth is still 75 nm. The control over feature dimensions with this process is excellent; the grating lines in resist began with a 75 nm linewidth, and this remained unchanged throughout all the process steps. Rounding of the lines after ion milling indicates that the W mask has worn more towards the edges than in the center. For thicker magnetic layers or narrower features, this taper of the etch mask could cause rapid narrowing of linewidths after a certain point in the etch. A similar problem was observed using Ti masks, described in Section 5.3 and seen most clearly in Fig. 5.5b. To extend the life of the tungsten masks, there are a couple of tricks that can be used to increase selectivity. One would be to take advantage of the low angular variation in W etch rates and etch the structures at an angle. Unfortunately, the equipment used for these experiments is not configured for this type of use. It has also been shown that changing the sputtering ion to a different noble gas can increase the selectivity of the etch [12].

The texturing seen between the grating lines in Figs. 5.9d,g is due the uneven clearing of the 2 nm chromium adhesion layer at the end of the etch. Areas which break through a bit earlier will begin to pit the underlying silicon substrate. Although it can be unsightly, this texturing is a good sign that the structures have not been over-etched. It can be confused for an incomplete etch at first glance, but the profile after stripping the remaining tungsten mask, Fig. 5.9e, proves this to be untrue. The etch chemistry for the W strip also happens to be near optimal chemistry for etching silicon, due to the high fluorine content of the plasma. Stripping the tungsten layer also has the effect of etching the underlying silicon, and the Co lines are seen to be resting atop short walls of Si. If the ion milling were incomplete, the Si etch would be impeded for areas with remaining metal and the

texturing would be enhanced. However, an Si etch is observed in Fig 5.9e, and the texturing is reduced at the bottom of the trench, indicating that all of the metal was cleared during the ion milling.

From a processing point of view, the thin phase-shifting resist stack in conjunction with tungsten hardmask is about as simple as possible. Consequently, it as the least likely to damage the heat sensitive multi-layer stacks used in GMR based MRAM devices. The two RIE steps are both fast, minimizing the total etch time, and can be cooled if necessary. The only baking step required is a 90 °C softbake to drive solvents out of the resist. Not only does the lack of an ARC eliminate a high temperature bake step, but it also eliminates the stripping step, usually done in an oxygen plasma, after etching the hardmask. This stripping step exposes the underlying magnetic material to the oxygen plasma, which can potentially damage both single films and multilayers by oxidation.
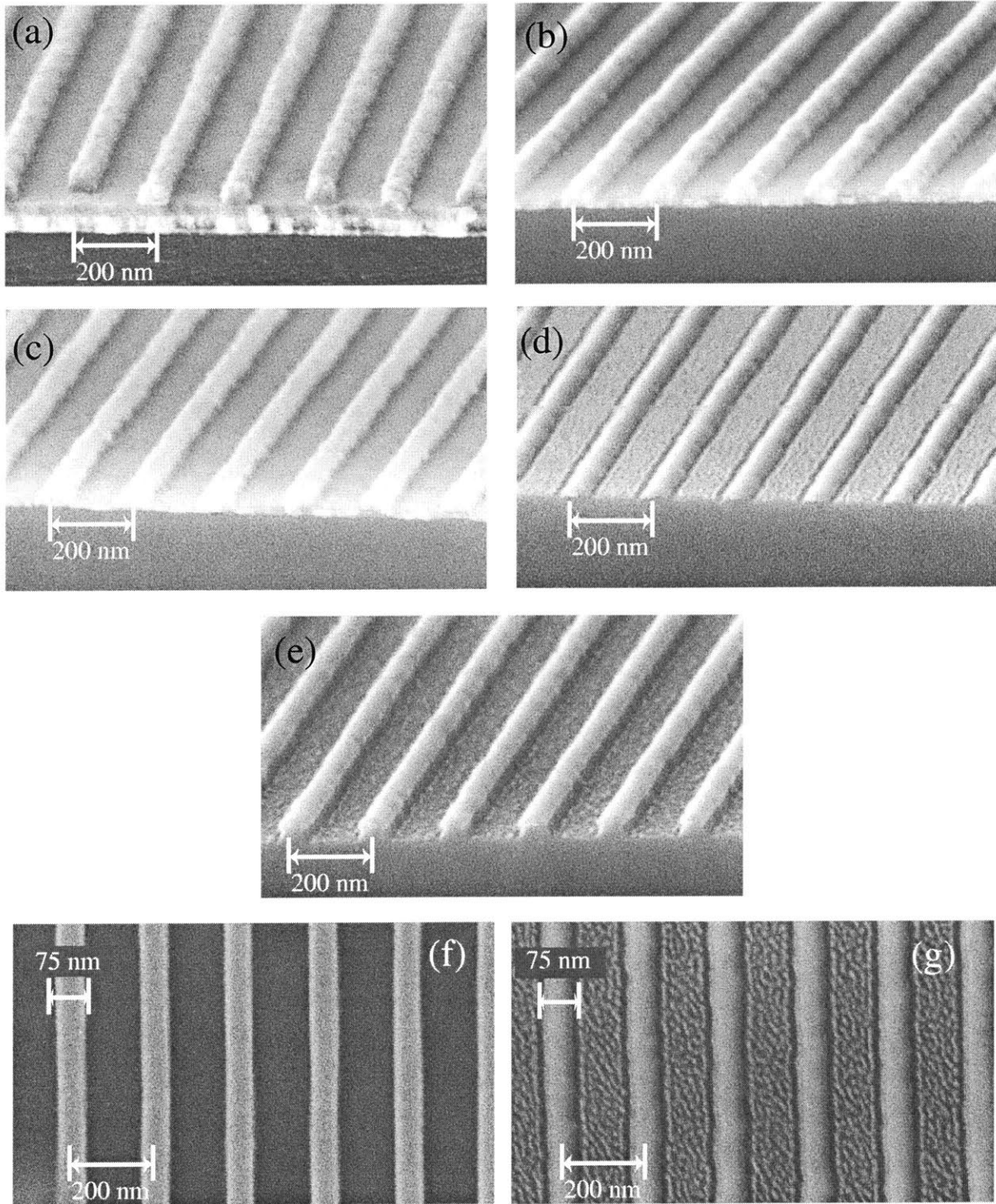
Figure 5.9: SEM micrographs of the thin phase-shifting resist process.

The simplicity of preparation of this stack in comparison with others is also very beneficial. When an ARC is used, the sequence of steps necessary to prepare the wafers can be quite tedious. The magnetic layers are sputtered on first, followed by the tungsten deposition either by sputtering or e-beam evaporation. Then the ARC is spun on and baked. Before the resist can be spun, the wafer must again go through an evaporation step to deposit the oxide interlayer. With the thin resist process, the magnetic layers, tungsten hardmask, and oxide phase shifting layer can all be deposited in sequence, either by sputtering or e-beam evaporation, without breaking vacuum. After this, the only remaining step is to spin the resist. The simplicity of the wafer preparation and etch sequence minimizes the chance of error for weary graduate students, which is among the more common modes of failure for any process.

One important feature of the thin phase-shifting resist mask is its compatibility with the entire variety of thin magnetic films. One of the functions of the ARC, as described in Chapter 2, was to isolate the exposure from the underlying substrate. Although the ARC has been eliminated, the W layer in the thin resist process provides the same degree of substrate isolation that could be expected with an ARC. The tungsten (n=3.99-2.56i at 325 nm), like other metals, can be thought of as a high index, highly absorbing layer. Light propagating through the tungsten is attenuated to the point that the optical properties of the underlying magnetic layers do not affect the exposure of the resist. Were this not the case, it would become very confusing if each different magnetic material required its own set of exposure parameters during lithography.

5.5) References

[1]   M.L. Schattenberg, R.J. Aucoin, and R.C. Fleming, "Optically matched trilevel resist process for nanostructure fabrication", J. Vac. Sci. Technol. B, **13** 3007, (1995)

[2]   R.E. Chapman, "Redeposition: a factor in ion-beam etching topography". J. Mater. Sci. **12** 1125 (1977)

[3]   H.R. Kaufman and R.S. Robinson, <u>Operation of Broad Beam Sources</u>. Commonwealth Scientific Corporation, Alexandria VA 1984.

[4]   O. Auciello, "Ion interaction with solids: Surface texturing, some bulk effects, and their possible applications". J. Vac. Sci. Technol. **19** 841 (1981)

[5]   D.R. Lide ed., <u>CRC Handbook of Chemistry and Physics, 73rd edition.</u> CRC Press, London, 1992

[6]   Y. Hao, M. Walsh, M. Farhuod, C.A. Ross, H.I. Smith, J.Q. Wang, L. Malkinski, "In-Plane Anisotropy in Arrays of Magnetic Ellipses". Submitted to IEEE Trans. Magn. for publication in September, 2000

[7]   Y. Hao, unpublished

[8]   Y. Hao, unpublished

[9]   G.K. Wehner and D.L. Rosenberg, "Angular Distibution of Sputtered Material", J. Appl Phys. **31** 177 (1960)

[10]   H.J. Lezec, E.H. Andersen, H.I. Smith, "An improved technique for resist-profile control in holographic lithography", J. Vac. Sci. Technol. B, **1** 1204, (1983)

[11]   N.N. Efremow, N.P. Economou, K. Bezijan, S.S. Dana, and H.I. Smith, "A simple technique for modifying the profile of resist exposed by holographic lithography", J. Vac. Sci. Technol., **19** 1234, (1981)

[12]   M.E. Walsh, Y. Hao, C.A. Ross and H.I. Smith, "Optimization of a Lithographic and Ion-Beam Etching Process for Nanostructuring Magneto-resistive Thin film Stacks", submitted for publication in J. Vac. Sci. Technol. B, **18** vol. 6, (2000)

Summary

Magnetic nanostructures were introduced in Chapter 1 as being one very promising candidate for next-generation data storage. However, limitations of current lithographic and etch technology are impeding progress towards bringing nanomagnet-based devices to market. Lithography and etching for the fabrication of sub-100 nm magnetic features are the two topics that comprise this thesis. Interference lithography (IL) is presented as a practical technique for printing sub-100 nm features over large areas. The use of anti-reflection coatings in interference lithography is investigated, and as is resist contrast. A simple, robust Lloyds-mirror interferometer was designed and constructed to facilitate research in nanomagnetics and other fields such as integrated optics. The Lloyds mirror interferometer is shown to have many advantages over the conventional IL architecture. Three methods for using IL to print features with in-plane shape anisotropy are presented and compared: dose modulation, off-orthogonal exposure, and dual-period exposure. The dual-period exposure in particular is something that is easy to implement with the Lloyds-mirror, but impractical with other interferometers.

Reactive-ion etching (RIE) and ion milling were compared as methods for high-resolution etching of magnetic materials and multilayer stacks. In a rare reversal of roles, ion milling is shown to be a more practical etch method than RIE for patterning thin magnetic films. The inherent problems of ion milling, notably low selectivity, faceting, and redeposition are found to arise only under certain conditions. Using this knowledge, a variety of resist stacks are analyzed with regard to linewidth control, redeposition, and process damage to magnetic materials and multilayers. The use of a thin hardmask is found to eliminate redeposition, and the choice of a material with low variation of etch rate with incident ion angle, such as tungsten, is found to be necessary to minimize faceting. A thin phase-shifting resist process is presented which simplifies processing and stack preparation, while also minimizing potential for heat-induced damage to magnetic multilayers. The combination of a thin resist stack with a tungsten hardmask is shown to be an optimal design for etching thin magnetic films. This research lays the groundwork for fabricating more complex magnetic devices, which should prove to be a fruitful area for continued investigation.

Appendix A

Reflectivity Simulation

The analogy between plane wave propagation and waves along an ideal transmission line is exact and complete. The concept of impedance matching in transmission line theory is the exact analogue of plane wave reflections at a material boundary[1]. For the problem of reflections from and in an arbitrary multi-layer structure, the transmission line formalism provides an intuitive and direct algorithm through the use of complex wave impedances. The recursive nature of the algorithm makes it ideal for implementation via a computer program, and the use of complex indices of refraction easily allows for both absorptive dielectrics and imperfect conductors.

For clarity, the case of normal incidence at a single boundary will be considered first and the theory then extended for oblique incidence and multiple layers. We begin by defining the orthogonal electric (E_x) and magnetic (H_y,) field quantities as a superposition of forward and reverse travelling plane waves.

$$E_x(z) = E_+ e^{-jkz} + E_- e^{+jkz} \qquad (A.1)$$

$$H_y(z) = H_+ e^{-jkz} - H_- e^{+jkz} \qquad (A.2)$$

The wavenumber k is defined in terms of the frequency ω and the permittivity ε and permeability μ.

$$k = \omega\sqrt{\mu \cdot \varepsilon} \qquad (A.3)$$

We also define a material property, the intrinsic impedance, in terms of the permeability and permittivity.

---

[1] S. Ramo, J.R. Whinnery, T. van Duzer, <u>Fields and Waves in Communication Electronics, 3rd Edition.</u> Wiley, New York (1994). This formalism can be traced to S.A. Schelkunoff, Bell Syst. Tech. J. **17** 17 (1938).

$$\eta = \sqrt{\frac{\mu}{\varepsilon}}$$ (A.4)

The wave impedance is defined for any plane z as the ratio of electric and magnetic field,

$$Z(z) = \frac{E_x(z)}{H_y(z)}$$ (A.5)

For the case of a single wave travelling in either the forward or reverse direction, the wave impedance is exactly equal to the intrinsic impedance of the material, $Z = \pm \eta$. However, in the presence of an impedance discontinuity caused by a material boundary, there will be both forward and reverse travelling components. The impedance in the second region is referred to as the load impedance, Z_L. In this case, the wave impedance is dependent on the distance l from the load impedance.

$$Z(l) = \eta \left[\frac{Z_L \cos(kl) + j\eta \sin(kl)}{\eta \cos(kl) + jZ_L \sin(kl)} \right]$$ (A.6)

The reflection of field quantities at the boundary (ρ) can be defined in terms of the load impedance and the intrinsic impedance of the incident material. It is interesting to note the prominent role of the intrinsic impedance of a material in determining reflection. Referring back to Equation A.4, both the dielectric properties (ε) and the magnetic properties (μ) are equally involved in determining η. Thus, although the magnetic properties of a material are often neglected, high values of μ will appreciably affect the reflectivity of that material. This should make intuitive sense if one recalls that propagating light consists of coupled electric and magnetic fields. High permeability materials affect the H field, which in turn affects the E field.

$$\rho = \frac{Z_L - \eta}{Z_L + \eta}$$ (A.7)

Reflected power is simply the square of this quantity, $R=(\rho)^2$.

When a plane wave is normally incident on a boundary, both the electric and magnetic fields are tangential to the boundary. In the case of oblique incidence, we can employ exactly the same results found for normal incidence if the impedance quantities are modified to only account for tangential components of E and H. Thus, the polarization of the light comes into play; TE and TM polarized waves will reflect differently.

$$\eta_{TM} = \eta \cos(\theta) \tag{A.8}$$

$$\eta_{TE} = \eta \sec(\theta) \tag{A.9}$$

The angle of incidence θ is measured from the normal, e.g. $\theta=0$ for normal incidence.

An arbitrary stack of materials is essentially a stack of impedance discontinuities. When this case is considered, the utility of this formalism becomes apparent. Until now, the concept of impedance has been no more or less useful than determining reflections using the index of refraction. To model a layered structure, we must assume that the incident layer and the final layer are semi-infinite, and that light is only incident from one side of the stack. Thus, in the final layer we can make the assumption that there is only a forward travelling wave. The impedance of the bottom layer in the stack will be only the intrinsic impedance of that material. Using this known quantity, we can work backwards up the stack solving for the actual impedance at each interface until the wave impedance at the top of the stack is found. This value is equal to the aggregate impedance of all the layers, and can be used in Equation A.7 to find the reflectivity off the entire stack.

Figure A.1 shows a simple 3-layer stack on a substrate with air as the incident medium. The load impedance of a given layer is shown to account for all the layers underneath. Working through this more specifically, we begin by letting the load impedance of the substrate layer equal the intrinsic impedance

of that material, $Z_{L0} = \eta_0$. At this point, one could calculate the reflection coefficient at this boundary, but it is unnecessary. Instead, we use Equation A.6 to convert the known impedance Z_{L0} into the load impedance at the top of the next lowest layer, Z_{L1}. Z_{L1} is then the total impedance for the combination of the substrate and layer 1. For TE waves, this would be

$$Z_{L1} = (\eta_1 \sec(\theta_1)) \left[\frac{Z_{L0} \cos(k_1 l_1) + j(\eta_1 \sec(\theta_1)) \sin(k_1 l_1)}{(\eta_1 \sec(\theta_1)) \cos(k_1 l_1) + jZ_{L0} \sin(k_1 l_1)} \right] \qquad (A.10)$$
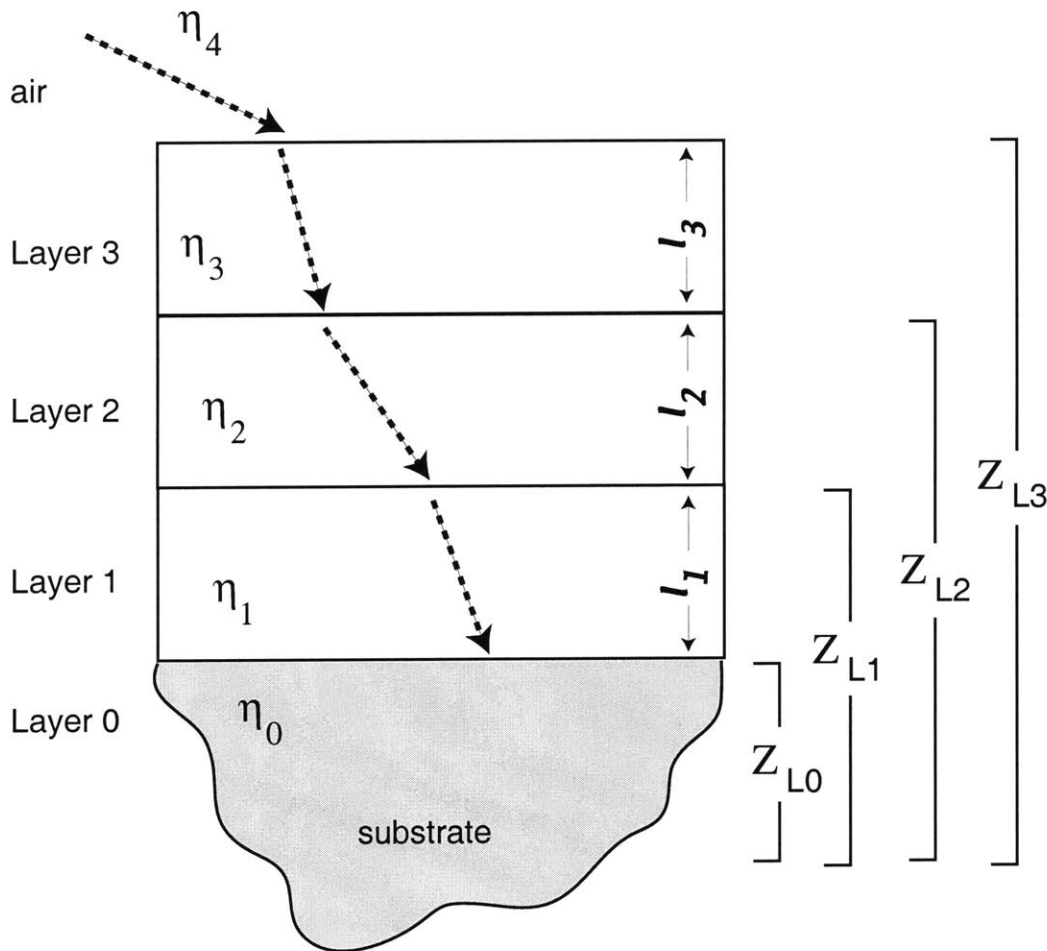

Figure A.1: *A multilayer stack with intrinsic and load impedances indicate. The load impedance at a given interface accounts for all layers underneath.*

Now, with Z_{L1} known, the problem is equivalent to one with 1 less layer and a substrate impedance of Z_{L1}. By recursively using Equation A.6 with the most recent load impedance, the known impedance value propagates up through the stack until the top layer is reached. The impedance Z_{L3} at the first material boundary is the impedance of the entire stack, and can be used in Equation A.7.

This method lends itself especially well to the application of interference lithography. Because a matrix of impedance values for every interface in the stack is found, the reflectivity at every interface in the stack is known. Thus, the reflectivity at both the top and bottom surfaces of the resist can be found using the same calculation. As mentioned in Chapter 2, both of these values are necessary for obtaining a good exposure.

The phase-shifting resist stack described in Section 5.4 also requires knowledge of the phase of the vertical standing wave formed in the resist. The reflection coefficients ρ found for any layer in the stack are complex, and thus can be written in polar form to emphasize magnitude and phase.

$$\rho = r \cdot e^{j\alpha} \qquad (A.11)$$

The phase portion of the reflectivity coefficient acts directly to influence the phase of the vertical standing wave. The vertical standing wave is formed from the interference of the incident and reflected components, so the intensity is proportional to the square magnitude of this sum.

$$I(z) \propto \left| e^{-jkz} + \rho e^{jkz} \right|^2 \qquad (A.12)$$

If Equation A.11 is expanded into a cosine, we get

$$I(z) \propto \left[(1 + r^2) + 2r \cdot \cos(2kz + \alpha) \right] \qquad (A.13)$$

Thus, all required information about the reflectivity properties of the resist stack can be found using the impedance propagation method.

A computer program was written using Matlab software which implements these calculations. The program is written based on matrix variables, rather than a scalar variables. Thus, any of the stack parameters can be made variable to investigate the sensitivity of the reflection coefficients as a function of such quantities as index of refraction, thickness or permeability. The required information to implement this algorithm is the complex index of refraction, permeability, and thickness for all layers. Table A.1 lists the indices of refraction for some common materials at 325 nm. In the context of interference lithography, the top layer is assumed to be air, and the bottom layer, usually a silicon wafer, is assumed to be semi-infinite. This assumption about the substrate is perfectly valid for highly reflective materials such as silicon. One instance where this might not be valid is when quartz wafers are used, as the substrate is transparent. Also, wavelength of the light and the incident angle in the first layer must be known. The angle of propagation in each of the subsequent layers can be easily calculated independently of the reflectivity calculation using Snell's Law.

Material	Complex Index of Refraction
PFI-88 resist	1.79-0.22i
ARC BARLi	1.55-0.14i
SiO_2	1.48
Silicon	4.68-2.03i
Alumina	1.8
Cobalt	1.3-2.33i
Nickel	1.69-1.99i
Copper	1.34-1.81i
Aluminum	0.326-3.95i
Chromium	1.12-2.95i
Titanium	1.68-2.25i
Tungsten	3.99-3.95i

Table A.1: *Complex indices of refraction at 325 nm wavelength for materials commonly encountered in the processing of magnetic thin films.*